



Tectonically assisted exhumation and cooling of Variscan granites in an anatectic complex of the Central Iberian Zone, Portugal: constraints from LA-ICP-MS zircon and apatite U–Pb ages

J. A. Ferreira¹ · T. Bento dos Santos¹ · I. Pereira² · J. Mata¹

Received: 13 February 2019 / Accepted: 13 July 2019 / Published online: 1 August 2019
© Geologische Vereinigung e.V. (GV) 2019

Abstract

Understanding the exhumation of middle to lower crustal rocks is of utmost importance to unravel intracrustal mass transfer processes during orogenic build-up. The Figueira de Castelo Rodrigo–Lumbrals Anatectic Complex (FCR–LAC) is located within the autochthonous terrane of the Variscan Central Iberian Zone and is an example of the association between S-type granites and migmatites. The anatectic complex contacts to the north and south with low-grade metamorphic units through the Huebra and Juzbado–Penalva do Castelo shear zones, respectively. Integration of new U–Pb zircon and apatite age data allowed us to obtain Variscan crystallization ages, inherited zircon ages and unprecedented cooling rates for different facies of the FCR–LAC granites. The zircon crystallization ages mostly cluster around 313–317 Ma for the syn-tectonic granites, whereas the dated late-tectonic granite provided an age of 300 Ma. The cooling rates range from 13 to 35 °C Ma⁻¹, which implies fast exhumation (0.3–0.84 mm a⁻¹) and shallow emplacement (ca. 8 km deep), compatible with exhumation facilitated by large crustal-scale shear zones. Inherited zircon in the granites reveals melting of Cadomian metasediments (650–550 Ma), Upper Cambrian–Lower Ordovician (495–470 Ma) metaigneous rocks (Ollo de Sapo formation) and of minor older components, suggesting protolith affinity with the Northern Domain of the Central Iberian Zone.

Keywords Iberian Variscan Orogeny · Syn-tectonic granites · U–Pb geochronology · Cooling rates · Exhumation rates

Introduction

Development of collisional orogens implies low-pressure–high-temperature (LP–HT) metamorphism, crustal anatexis and generation of crustal-derived granitic magmas as late-stage features (e.g. Žák et al. 2011). The study of granitic magmatism is, of great importance to understand the evolution of orogenic belts, providing information regarding

the interactions between magmatism and tectonics, as well as intracrustal heat and mass transfer processes.

The Variscan orogenic belt in Europe is a collisional orogen that developed during the complex collision of the Laurussia and Gondwana continents during the Devonian and Carboniferous periods (e.g. Nance et al. 2010; Kroner and Romer 2013). Along the European Variscan Belt, the initial continental collision and related crustal thickening precede the formation of metamorphic core complexes characterized by exhumed mid-crustal migmatites, LP–HT metamorphism and large volumes of granitic magmas (Schulmann et al. 2002, 2008; Žák et al. 2011; Villaros et al. 2018).

Large volumes of granites can also be found in the Iberian Variscan Belt, particularly in the Central Iberian Zone (CIZ), (Ferreira et al. 1987; Dias et al. 1998; Villaseca et al. 1998; Azevedo and Valle Aguado 2013; Valle Aguado et al. 2017; Dias da Silva et al. 2018), a zone which has been interpreted as a section of the Gondwana margin partially underlying a set of allochthonous tectonic slices of continental and oceanic affinities (e.g., Ribeiro et al. 2007; Arenas et al. 2016; Mateus et al. 2016). In the CIZ, granitic plutons

Electronic supplementary material The online version of this article (<https://doi.org/10.1007/s00531-019-01755-1>) contains supplementary material, which is available to authorized users.

✉ J. A. Ferreira
jaferreira@fc.ul.pt

¹ IDL-Instituto Dom Luiz, Faculdade de Ciências, Universidade de Lisboa, Campo Grande, 1749-016 Lisbon, Portugal

² School of Earth and Environmental Sciences, University of Portsmouth, Building Burnaby Rd, Portsmouth P01 3QL, UK

were emplaced after the first Variscan compressive event and Barrovian metamorphism, being usually interpreted as the result of syn-orogenic collapse (Escuder-Virueite et al. 1994; Valle Aguado et al. 2005; Dias da Silva et al. 2017). However, some of these complexes are associated with strike-slip shear zones (e.g., Costa et al. 2014; Pereira et al. 2017) raising an interesting and unsolved question concerning the role of the shear movements in the exhumation of anatectic complexes and, consequently, in the timing of the generation and emplacement of the associated Variscan granites during the intracontinental collision stages.

This study focuses on the granites within the Figueira de Castelo Rodrigo–Lumbrals Anatectic Complex (FCR–LAC), constrained by a major strike-slip shear zone: the Juzbado–Penalva do Castelo Shear Zone (JPCSZ; Iglesias and Ribeiro 1981). The FCR–LAC has been the target of recent studies that partially constrained its evolution (Díez Fernández and Pereira 2016, 2017; Pereira et al. 2017; Alves Ribeiro et al. 2017). However, for the complete understanding of this complex, it is still necessary to characterize/quantify the emplacement conditions of these anatectic granitic bodies, namely through the determination of crystallization ages and exhumation rates. Indeed, to date, and besides some past geochronological studies using K–Ar and Rb–Sr methods (Macedo 1988; Ribeiro 2001), only two studies presented U–Pb ages for granites of this complex (Díez Fernández and Pereira 2017; Pereira et al. 2018) although 10 distinct intrusive facies have been described (Ribeiro 2001).

The main objective of this work is to present new U–Pb zircon and apatite ages for distinct FCR–LAC granite facies with the purpose of, for the first time, constrain their crystallization ages and cooling rates, and, therefore, their emplacement conditions within the framework of the Variscan Orogeny. This innovative study aims to bring a better understanding for the tectono-metamorphic evolution of the internal zone of the Iberian Variscides, as well as for the role of intracontinental first-order shear zones in the exhumation of deep settled rocks in collisional orogens worldwide.

Geological setting

The Figueira de Castelo Rodrigo–Lumbrals Anatectic Complex

The Gondwana–Laurussia continental collision sets the beginning of the Variscan orogeny, being responsible for the tectonometamorphic evolution of the Iberian Massif from the Upper Devonian to the late Carboniferous (e.g. Matte 1991; Ribeiro et al. 2007). The effects of continental collision in the Central Iberian Zone (CIZ), started at ca. 370–360 Ma and led to multistage deformation and metamorphic events (Dallmeyer et al. 1997; Martínez Catalán

et al. 2014; Dias da Silva et al. 2017; Díez Fernández and Pereira 2017; Pastor-Galán et al. 2019). Three regional tectono-metamorphic events have been identified in the CIZ (e.g., Valle Aguado et al. 2017, and references within): (1) The D_1 deformation phase, caused crustal thickening/shortening and Barrovian metamorphism between 365 and 340 Ma (Dallmeyer et al. 1997); (2) The local D_2 extensional phase (340–320 Ma; e.g., Martínez Catalán et al. 2014; Gutiérrez-Alonso et al. 2018, and references within) produced flat-lying extensional detachments and related low-dipping foliation preserved in low- to high-temperature/low-pressure metamorphic rocks, including migmatites (see Rodrigues et al. 2013; Dias et al. 2016 and Pereira et al. 2017 for alternative interpretations); (3) the D_3 phase favoured the reactivation of several first-order transcurrent shear zones, the emplacement of crustal-derived melts (320–295 Ma; Valle Aguado et al. 2017) and regional retrograde metamorphism, synchronous with regional uplift (e.g., Martínez Catalán et al. 2014).

The FCR–LAC, located in the Iberian Variscan Belt within the autochthonous terrains of the CIZ (Fig. 1), is an anatectic complex composed of migmatites (metatexites and diatexites) that are gradually transforming into S-type, two-mica granites with several distinct facies, that can be differentiated by grain size and by the relative abundance of micas (muscovite and biotite) (Fig. 2a, b). The different facies were named I γ to X γ , from oldest to youngest, and their distinction was based on deformation and field relationships (Ribeiro 2001). Some granitic plutons (e.g., I γ) reveal deformation structures concordant with the direction of the Juzbado–Penalva do Castelo shear zone supporting its syn-kinematic nature.

Granitic plutons outcropping in the FCR–LAC have been previously dated yielding a K–Ar age of 319 ± 6 Ma (Macedo 1988) and an U–Pb age of 307.8 ± 3.1 Ma for the São Pedro-Vieiro granite (Díez Fernández and Pereira 2017), as well as an U–Pb age of 318.7 ± 4.8 Ma for the Mêda-Escalhão-Penedono granite (Pereira et al. 2018). The FCR–LAC extends to Spain where the Lumbrals granite, yielded a Rb–Sr whole-rock age of 300 ± 8 Ma (García Garzon and Locutura 1981) re-estimated in 311.2 ± 3.7 Ma using $^{40}\text{Ar}/^{39}\text{Ar}$ step-heating micas (Roda-Robles et al. 2009, 2018; Vieira 2010).

Associated with the S-type, two-mica granites occur metatexites and diatexites forming together an anatectic complex. The metatexites exhibit stromatic textures, and occasionally it is noticeable centimetric to millimetric layers of peritectic sillimanite associated with muscovite (Fig. 2c). At times, the metatexites are intersected by leucosomatic veins or pockets of granitic, pegmatitic or diatexitic material. Diatexites show restitic nodules (Fig. 2d), schlieren structures, and, occasionally, ptygmatic folding. When near local shear zones, the diatexites reveal a steep foliation

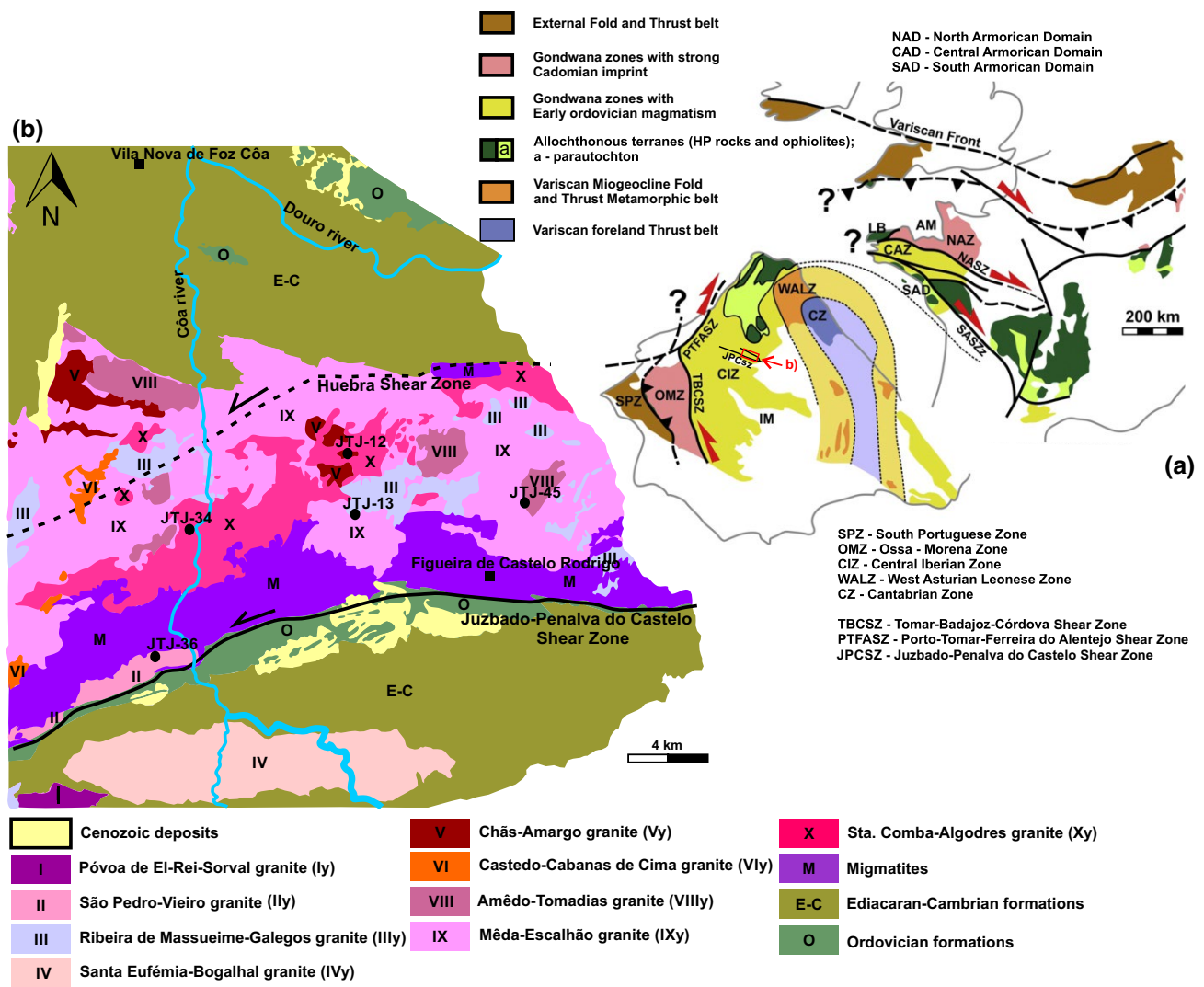


Fig. 1 a Location of the studied area in the Iberian Massif context (modified from Dias et al. 2016); b geological map of the Figueira de Castelo Rodrigo–Lumbrales Anatectic Complex (modified from Silva and Ribeiro 2000)

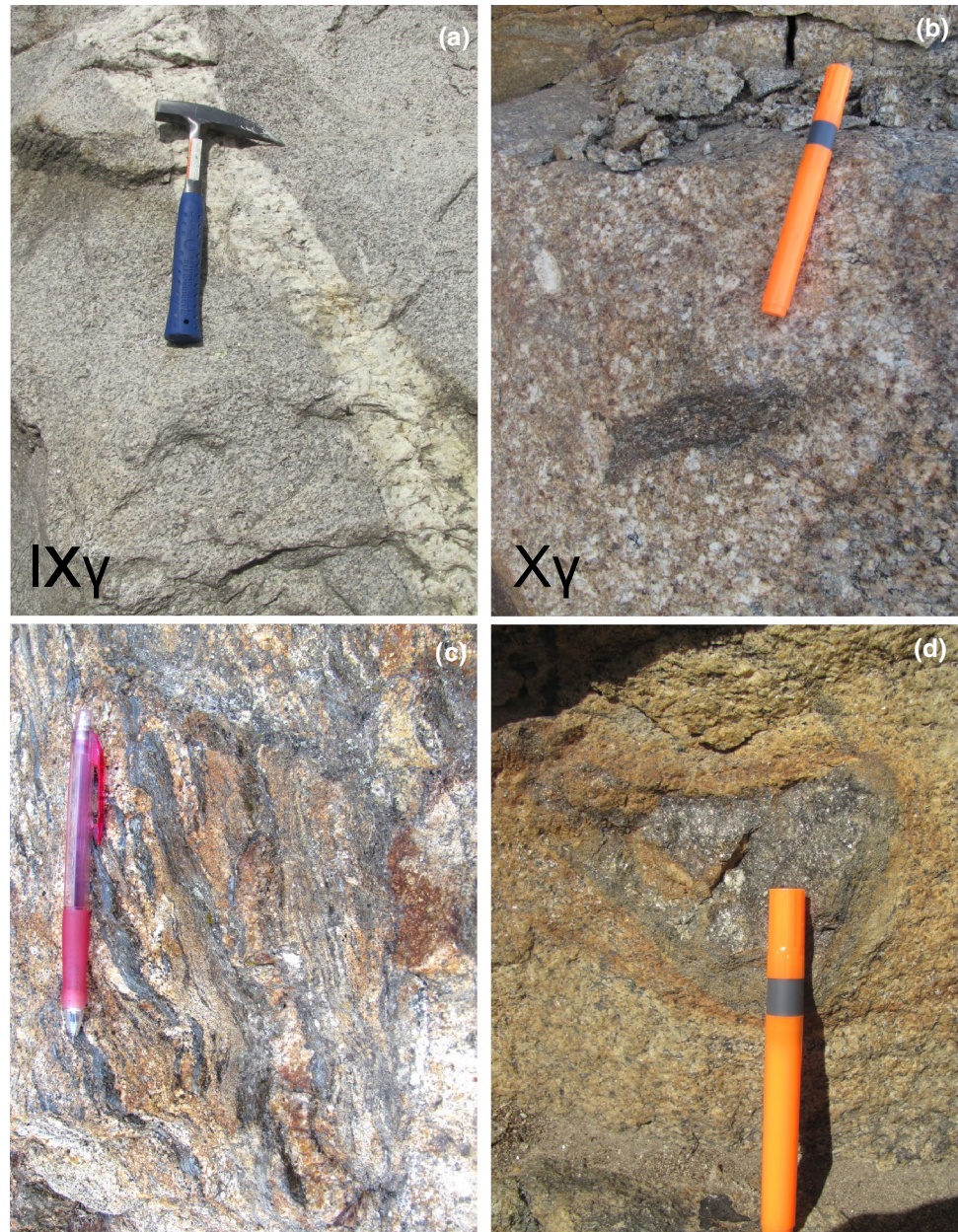
parallel to the shear direction (E–W). Nebulitic textures in diatexites are also occasionally present.

The anatectic complex is 5–15-km wide, delimited by two sinistral, east–west to ENE–WSW trend, first-order shear zones (Fig. 1) that juxtapose the complex onto the low-grade metamorphic units of the Ediacaran–Cambrian Douro-Beiras Supergroup (Sousa and Sequeira 1993) and the Ordovician Armorican Quartzites (Sá et al. 2005; Gutiérrez-Alonso et al. 2007). These two sinistral shear zones that limit the FCR–LAC are the Huebra Shear Zone at the North, and the Juzbado–Penalva do Castelo Shear Zone to the South (Iglesias and Ribeiro 1981; Pereira et al. 2017). The JPCSZ extends for 200 km and its sinistral displacement took place at least during the D₃ intracontinental collision stage (Iglesias and Ribeiro 1981; Villar Alonso et al. 2000; Pereira et al. 2017). The last activity

of this strike-slip shear zone was dated at 309 ± 2.5 Ma (⁴⁰Ar/³⁹Ar on synkinematic white micas), in the eastern part of it (in Juzbado; Gutiérrez-Alonso et al. 2015). Recently, Valle Aguado et al. (2017) suggested that the JPCSZ movement in the western termination ceased during the emplacement of the late-tectonic Viseu batholith at ca. 299 Ma (U–Pb zircon ages), indicating diachronism in the shearing propagation.

The JPCSZ has been suggested to have played an important role for the exhumation of the FCR–LAC with an estimated minimum vertical displacement of 7–13 km and a horizontal displacement of 65–100 km by simple shear-dominated transpression during the Variscan D₃ orogenic events (Pereira et al. 2017). Yet, it is still not clear when anatexis took place and what mechanisms controlled the genesis and final emplacement of the anatectic complex.

Fig. 2 **a** Medium-grained, two-mica granite ($IX\gamma$) intruded by a pegmatitic vein; **b** fine-grained, porphyritic granite ($X\gamma$); **c** metatexite exhibiting stromatic texture; **d** diatexite including a restitic nodule



Sample description and analytical techniques

Sample description

Granite samples were collected within the FRC–LAC at the localities indicated in Fig. 1. The $II\gamma$ granite crops out between the migmatite belt and the JPCSZ, elongated accordingly with the shear-zone direction (WSW–ENE). This muscovite > biotite granite is fine-grained and reveals meso- and microscopic deformation. The mineral assemblage is defined by quartz + plagioclase + muscovite + biotite ± orthoclase ± chlorite ± zircon ± apatite ± opaque minerals. The $III\gamma$

granite has a porphyroid texture (feldspar megacrysts) within a medium grain-size matrix. It is composed by quartz + plagioclase + microcline + biotite + muscovite ± orthoclase ± fibrolitic sillimanite ± zircon ± apatite ± opaque minerals. The $V\gamma$ granite is a biotite > muscovite facies and it has a coarse-grained texture. The mineral assemblage of this granite consists in quartz + plagioclase + potassic feldspar + biotite + muscovite ± chlorite ± fibrolitic sillimanite ± zircon ± apatite ± opaque minerals. The $IX\gamma$ granite is the most representative facies in the study area. Its grain size ranges between fine- and coarse-grained. The mineral assemblage is represented by quartz + plagioclase + potassic feldspar + biotite + muscovite ± chlorite ± fibrolitic

sillimanite ± zircon ± apatite ± rutile ± opaque minerals. The X γ granite is a muscovite > biotite granite, essentially coarse-grained, at times exhibiting a porphyroid fine-grained texture. Its mineral assemblage is composed of quartz + plagioclase + microcline + muscovite + biotite ± orthoclase ± chlorite ± fibrolitic sillimanite ± zircon ± apatite ± rutile ± opaque minerals.

Analytical techniques

All samples were prepared for the different types of analytical procedures at the Mineral Separation Lab of GeoF-CUL—Department of Geology of the University of Lisbon. Zircon and apatite crystals were picked from a 63- to 250- μ m fraction, after heavy liquid and electromagnetic separation.

Grains, mounted in epoxy resin mounts, were attached to metallic stubs with thin copper strips, and coated with a 1-nm pulverized gold film. Zircon and apatite grains were observed using a ZEISS EVO10MA scanning electron microscope (SEM) at the University of Portsmouth (UoP). For backscatter electron (BSE) imaging, an accelerating voltage of 20 kV and 700 pA beam current was applied to reveal internal structures in the analyzed grains.

U–Pb isotopic analyses were performed using an ASI RESOLUTION 193 nm ArF excimer laser coupled to the ANALYTIK JENA Plasma Quant Elite quadrupole ICP-MS at UoP. The detailed instrumental setup and ablation conditions can be found in Supplementary Material. For zircon U–Pb dating, a beam spot size of 20 μ m (cores) and 11 μ m (smaller grains and rims) was preferred. Beam energy densities used ranged from 2.1 to 2.5 J cm⁻², with a 2-Hz repetition rate. As for apatite, a beam spot size between 50 and 20 μ m was used, with beam energy densities ranging from 2.8 to 3 J cm⁻², and a 3-Hz repetition rate. For additional information on the analytical conditions used for the LA-ICP-MS analyses, see Supplementary Material 1.

Plešovice was used as a primary standard for zircon (337.13 ± 0.13 Ma; Sláma et al. 2007) whereas the Madagascar standard was used for apatite (473.5 ± 0.7 Ma; Thomson et al. 2012). 91500 (1062.4 ± 0.4 Ma; Wiedenbeck et al. 1995), and GJ1 (608.5 ± 0.4 Ma; Jackson et al. 2004) were used as zircon secondary standards, whereas for apatite were used McClure (523.51 ± 2.09 Ma; Schoene and Bowring 2006) and Xuxa (unpublished, ca. 572 Ma, provided by courtesy of C. Lana, Federal University of Ouro Preto) (see Supplementary Material 2). For all the above, reproducibility of the secondary standards was within 2%.

IOLITE 3.31 software package was used for data reduction. A sample-standard bracketing method was used to correct for both instrumental drift and elemental mass fractionation.

For zircon, Wetherill concordia and weighted mean ²³⁸U/²⁰⁶Pb ages were calculated using ISOPLOT/EX 4.1

(Ludwig 2003). From the youngest zircon population data, only grains that were 95–105% concordant were used to determine crystallization ages.

For apatite, the isotopic data was processed using Vizual-Age_UcomPbine DRS and measured ²⁰⁷Pb (Chew et al. 2014). This data reduction scheme allows for common-Pb (Pb_{cm}) correction of the primary standard based on their known radiogenic and variable Pb_{cm} compositions. This correction is then applied to the unknowns.

Apatite Tera–Wasserburg concordia ages were determined using ISOPLOT/EX 4.1 (Ludwig 2003).

Trace element analyses in zircon were performed using the same instrument setup as for U–Pb, and a standard-sample bracketing method to correct for instrumental drift. The following isotopes were analyzed: ²⁹Si, ³¹P, ³⁹K, ⁴⁰Ca, ⁴⁵Sc, ⁴⁹Ti, ⁵¹V, ⁵²Cr, ⁵⁵Mn, ⁸⁵Rb, ⁸⁷Sr, ⁸⁹Y, ⁹⁰Zr, ⁹³Nb, ⁹⁵Mo, ¹¹⁸Sn, ¹²¹Sb, ¹³³Cs, ¹³⁷Ba, ¹³⁹La, ¹⁴⁰Ce, ¹⁴¹Pr, ¹⁴⁶Nd, ¹⁴⁷Sm, ¹⁵³Eu, ¹⁵⁷Gd, ¹⁵⁹Tb, ¹⁶³Dy, ¹⁶⁵Ho, ¹⁶⁶Er, ¹⁶⁹Tm, ¹⁷²Yb, ¹⁷⁵Lu, ¹⁷⁷Hf, ¹⁸¹Ta, ¹⁸²W, ²⁰⁸Pb, ²⁰⁹Bi, ²³²Th and ²³⁸U.

A laser beam diameter of 40 μ m for NIST612, 35 μ m for secondary standards and 35–25 μ m for unknowns was used, with beam energy densities ranging from 3.8 to 4.1 J cm⁻², with a 4-Hz repetition rate (Supplementary Material 1). NIST612 was used as primary standard using concentrations by Jochum et al. (2011), whereas 91500 (Wiedenbeck et al. 1995) and GJ1 (Jackson et al. 2004) were used as secondary standards, as they are relatively homogenous in terms of trace element concentrations. Zr was used as an internal calibration standard, considering zircon stoichiometry (Zr = 43.1 wt%). Most analyzed elements are within 10% and 5% accuracy relative to secondary standards published values, and ⁴⁹Ti is within 10% uncertainty of reported values (see Supplementary Material 2), excluding uncertainties, with a detection limit of 3 ppm.

Results

Zircon U–Pb ages

U–Pb zircon ages were obtained for five of the granite facies from the FCR–LAC defined by Ribeiro (2001) (Fig. 1; Table 1): São Pedro-Vieiro (II γ), Ribeira de Massueime-Galegos (III γ), Chás-Amargo (V γ), Mêda-Escalhão (IX γ) and Sta. Comba-Algodres granite (X γ).

Zircon external morphology has been widely used in petrogenetic studies, particularly those targeting granitoids (e.g., Pupin 1980; Barbarin 1988; Belousova et al. 2006; Köksal et al. 2008). Zircon morphology depends on the crystallization rate, fluid composition and on the temperature of the crystallization medium (Corfu et al. 2003). Pupin (1980) established a systematics for zircon using the relative development of the prismatic and pyramidal crystal forms,

Table 1 LA-ICP-MS U–Pb zircon data of the Figueira de Castelo Rodrigo–Lumbrales anatectic complex granites

Id	U (ppm)			Th (ppm)			Th/U	Common-lead uncorrected			Final ages (Ma)			Concordance (%) ^b	
		$\pm 2\sigma$	$^{206}\text{Pb}/^{238}\text{U}$		$\pm 2\sigma$	$^{206}\text{Pb}/^{238}\text{U}$		$^{207}\text{Pb}/^{235}\text{U}$	$\pm 2\sigma$	$^{206}\text{Pb}/^{238}\text{U}$	$\pm 2\sigma$	$^{207}\text{Pb}/^{235}\text{U}$	$\pm 2\sigma$		$^{207}\text{Pb}/^{206}\text{Pb}$
São Pedro-Vieiro granite (IIγ) lat: 40.853; long: – 7.132															
M7_36_4c	273	94	0.34	0.336	0.016	0.0468	0.00089	0.0009	292	12	295	6	235	93	101
M7_36_11c	819	54	0.07	0.355	0.013	0.04742	0.00076	0.0008	308	10	299	5	354	71	97
M7_36_18c	377	104	0.28	0.344	0.015	0.0478	0.00086	0.0009	299	11	301	5	259	88	101
M7_36_5c	312	170	0.54	0.354	0.015	0.04826	0.00086	0.0009	307	11	304	5	295	86	99
M7_36_3e	383	125	0.33	0.341	0.021	0.0472	0.0012	0.03	293	16	297	7	230	130	102
Ribeira de Massuime-Galegos granite (IIIγ) lat: 40.917; long: – 7.011															
M5_13_2b	1489	26	0.02	0.369	0.038	0.0502	0.0012	0.18	316	28	316	7	263	190	100
M5_13_1c	1163	39	0.03	0.370	0.038	0.0508	0.0012	0.29	317	28	320	7	252	180	101
M7_13_15e	1195	69	0.06	0.348	0.011	0.0489	0.0011	0.13	301	8	308	7	337	76	102
M5_13_2c	737	9	0.01	0.3684	0.0084	0.05	0.0007	0.0007	318	6	314	4	323	48	99
Chás-Amargo granite (Vγ) lat: 40.944; long: – 7.014															
M6_12_6e	1369	323	0.24	0.37	0.03	0.0516	0.0012	0.23	318	23	325	7	235	170	102
M6_12_2e	1285	6	0.005	0.36	0.03	0.0506	0.0012	0.18	313	22	318	8	248	180	102
M6_12_1c	1638	186	0.11	0.361	0.015	0.049	0.001	0.001	313	12	311	6	307	98	99
M6_12_19e	757	7	0.01	0.361	0.031	0.049	0.0012	0.33	310	23	308	8	280	180	99
M1_12_6	2479	24	0.01	0.382	0.015	0.05029	0.00058	0.0006	328	11	316	4	436	74	96
Mêda-Escalhão granite (IXγ) lat: 40.923; Long: – 6.91															
M6_45_3e	1158	152	0.13	0.363	0.029	0.0504	0.0012	0.25	313	22	317	7	258	180	101
M4_45_8c	10890	44	0.004	0.3658	0.0059	0.0505	0.0015	0.48	316	4	318	9	285	32	101
M4_45_2	2570	256	0.10	0.3678	0.0055	0.05082	0.00067	0.0007	318	4	320	4	303	27	100
M6_45_1c	1215	117	0.10	0.364	0.016	0.05	0.001	0.001	316	12	313	6	327	99	99
Sta. Comba-Algodres granite (Xγ) Lat: 40.911; long: – 7.11															
M6_34_15c	1624	327	0.20	0.364	0.015	0.049	0.001	0.001	314	11	307	6	364	97	98
M6_34_11c	1543	353	0.23	0.349	0.015	0.04894	0.00099	0.001	303	11	308	6	254	97	102
M6_34_15e	2304	629	0.27	0.364	0.0098	0.04901	0.00069	0.11	314	7	308	4	317	61	98
M6_34_10e	951	64	0.07	0.356	0.013	0.04919	0.00068	0.29	307	10	310	4	256	74	101
M6_34_29e	1662	220	0.13	0.351	0.028	0.0492	0.0011	0.16	305	21	310	7	253	180	102
M6_34_26c	815.2	159	0.19	0.381	0.017	0.049	0.001	0.001	327	12	311	6	426	100	95
M6_34_30e	1742	271	0.16	0.369	0.029	0.0495	0.0012	0.30	318	21	312	7	340	170	98
M6_34_1e	2146	15230	7.10	0.3789	0.0099	0.04964	0.00064	0.20	325	7	312	4	369	56	96
M6_34_11e	1471	191	0.13	0.35	0.01	0.04971	0.00068	0.21	300	8	313	4	195	63	104
M6_34_23c	1256	198	0.16	0.366	0.016	0.05	0.001	0.001	317	12	313	6	329	100	99
M6_34_10c	1882	38	0.02	0.382	0.016	0.05	0.001	0.001	328	12	313	6	426	97	95

Table 1 (continued)

Id	U (ppm)	Th (ppm)	Th/U	Common-lead uncorrected		Final ages (Ma)		Concordance (%) ^b							
				²⁰⁷ Pb/ ²³⁵ U ± 2σ	²⁰⁶ Pb/ ²³⁸ U ± 2σ	²⁰⁷ Pb/ ²³⁵ U ± 2σ	²⁰⁶ Pb/ ²³⁸ U ± 2σ								
M6_34_14e	1635	335	0.20	0.37	0.012	0.0498	0.0006	0.15	318	9	314	4	299	68	99
M6_34_14c	1195	90	0.08	0.364	0.016	0.05	0.001	0.001	315	12	315	6	295	98	100
M6_34_24e	2004	17	0.01	0.363	0.029	0.05	0.0012	0.31	313	21	315	7	288	170	100
M6_34_27c	1080	3950	3.66	0.373	0.016	0.05	0.001	0.001	321	12	315	6	348	99	98
M6_34_5e	1623	225	0.14	0.370	0.012	0.05038	0.00068	0.28	318	9	317	4	274	66	100
M6_34_25c	1254	2210	1.76	0.375	0.016	0.05	0.001	0.001	323	12	318	6	344	100	98
M6_34_13c	1508	249	0.16	0.364	0.016	0.051	0.001	0.001	316	11	318	6	272	98	101
M6_34_33c	908	165	0.18	0.379	0.017	0.051	0.001	0.001	325	13	318	6	357	100	98
M6_34_22c	1308	173	0.13	0.374	0.016	0.051	0.001	0.001	322	12	320	6	320	100	99

^aRho is calculated by Iolite package software and it corresponds to the correlation between the given errors of the ²⁰⁷Pb/²³⁵U and ²⁰⁶Pb/²³⁸U ratios

^bConcordance = (²⁰⁶Pb/²³⁸U age)/(²⁰⁷Pb/²³⁵U age) × 100

considering the development of prismatic faces mainly related with the temperature of crystallization and the pyramidal faces with chemical factors. These parameters inferred from a zircon population can be helpful to characterize the evolution of a magma system (Corfu et al. 2003). However, the morphology systematics proposed by Pupin (1980) has been questioned by several authors (e.g., Vavra 1990, 1993; Benisek and Finger 1993) which advocate that the zircon morphologies can only reflect the latest stages of growth. Sometimes, it is possible to distinguish igneous and metamorphic zircon from its morphology. In general, euhedral, concentric oscillatory zoning and euhedral, prismatic external morphology are evidences for igneous zircons. Zircon from a high-grade metamorphic environment can exhibit patchwork zoning and multifaceted, equant, tabular external morphology (e.g., Aleinikoff et al. 2006). However, at very high metamorphic grade, these morphological distinctions related with the origin (igneous vs. metamorphic) are not so clear, especially under anatectic conditions (Aleinikoff et al. 2006). Th/U ratios has also been used to distinguish metamorphic (< 0.1) and magmatic (> 0.1) zircons (e.g., Williams et al. 1996; Rubatto and Gebauer 2000), yet its use for such purpose is debatable (see Discussion).

Considering all these mentioned features, the selection of zircon grains for dating was made taking into account the maximum number of characteristics that was possible to determine/observe.

São Pedro-Vieiro granite (Ily)

Zircon morphology of the São Pedro-Vieiro granite varies among elongated prismatic and oval shape (Fig. 3a). Occasionally, zircon grains show the development of bipyramidal terminations (most of them 211), whereas others have one pyramid developed in one direction and the opposite edge is rounded. About the zircon prisms, most of them are 100. Regarding zircon internal morphology, oscillatory zoning is rare. All zircon crystals have narrow rims (2–18 μm), but most of them depicting an unzoned core and intermediate zones. At times, a few zircons appear fractured. The Th/U ratio ranges from 0.07 to 0.54.

From this granite, we analyzed 22 zircon grains for U–Pb. From 5 younger zircon cores (Table 1) yielding 300 ± 2.2 Ma (MSWD = 1.4) (Fig. 4a), we determined the crystallization age of the Ily granite, significantly younger than the K–Ar crystallization age (319 ± 6 Ma) obtained by Macedo (1988).

Recently, Díez Fernández and Pereira (2017) obtained a SHRIMP U–Pb zircon age of 307.8 ± 3.1 Ma (MSWD = 1.8) for the São Pedro-Vieiro granite, which is slightly older than our estimate and outside analytical uncertainty of our measurement.

Eleven zircon grains with concordant inherited cores yield dates ranging from Lower Devonian (400 Ma) to

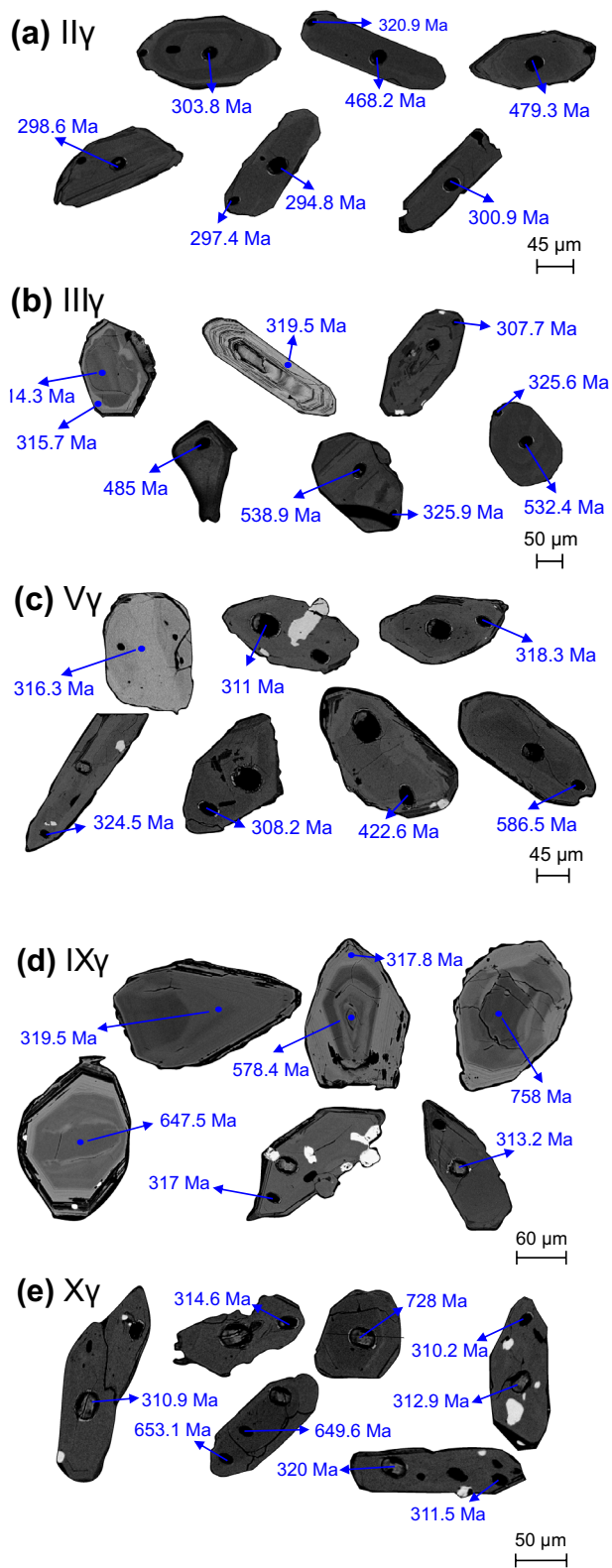


Fig. 3 Back-scattered electron images of representative zircon grains of the five studied granites: **a** São Pedro-Vieiro granite (II γ); **b** Ribeira de Massueime-Galegos granite (III γ); **c** Chãs-Amargo granite (V γ); **d** Mêda-Escalhão granite (IX γ); **e** Sta. Comba-Algodres granite (X γ)

Paleoproterozoic (2000 Ma) (Table 2). From the inherited zircon cores, it was observed 4 younger overgrowths with Variscan age.

Ribeira de Massueime-Galegos granite (III γ)

In general, the Ribeira de Massueime-Galegos granite contains prismatic zircon, although a few crystals have acicular shape with oscillatory zoning and others have oval shapes with rounded terminations. When the oscillatory zoning is present, it is more visible in the thin zircon rims (5–18 μ m) surrounding the unzoned cores and, quite rarely, the cores appear with convoluted zoning (Fig. 3b). This feature is typical of zircon growing during high-temperature metamorphism (Corfu et al. 2003). The majority of the zircon grains have 211 pyramids and 100 prisms, and sometimes they appear fractured. The Th/U ratios are low, ranging from 0.01 to 0.06.

The ablation was done in 22 grains of the III γ granite. The young concordant dates (Table 1) (1 core and three rims) allowed to estimate the 314.1 ± 2.6 Ma (MSWD=0.12) crystallization age for this granite (Fig. 4b). Five old zircons provided Cambrian and Ediacaran ages around 485–600 Ma (Table 2).

Chãs-Amargo granite (V γ)

Zircon grains from the Chãs-Amargo granite have prismatic and oval morphology, sometimes with rounded terminations and narrow rims (4–18 μ m) (Fig. 3c). The zircon typology is heterogeneous, since the pyramids range between 211 and 101, and prisms between 110 and 100. The Th/U ratio varies between 0.005 and 0.24.

Thirty zircon grains were analyzed and it was determined a date of 316.2 ± 3.9 Ma (MSWD=1.10) for the V γ granite, using 5 younger zircons (Table 1) (4 cores and 1 rim), which is ascribed as its crystallization age (Fig. 4c). From the 30 grains, 16 of them correspond to older concordant dates with ages from Lower Devonian (400 Ma) to Paleoproterozoic (2500 Ma) (Table 2).

Mêda-Escalhão granite (IX γ)

The Mêda-Escalhão granite carries prismatic zircon grains, at times with planar or oval shape. Many crystals have the pyramids developed in one direction and occasionally, they appear fractured. In addition, they have thin rims and faint zoning in both cores and rims (3–26 μ m) (Fig. 3d). Most of the zircon grains exhibit 211 pyramids and 100 prisms. The Th/U ratio fluctuates between very low values of 0.004 and 0.13.

The U–Pb dating was carried out on 23 grains. From 4 younger zircon grains (Table 1) (3 cores and 1 rim) was

determined a date of 317.4 ± 2.1 Ma (MSWD = 0.097) that corresponds to the crystallization age of the IX γ granite (Fig. 4d).

Pereira et al. (2018) dated this granite facies (Mêda-Escalhão-Penedono massif) to the west of the FCR–LAC, estimating a LA-ICP-MS U–Pb zircon age of 318.7 ± 4.8 Ma (MSWD = 0.22) which is in agreement with the age obtained in this study, within error.

Five concordant old cores stand out, from the group of 23 grains, showing Cambrian and Cryogenian ages from 500 to 750 Ma (Table 2).

Sta. Comba-Algodres granite (X γ)

Most of the zircon that compose the Sta. Comba-Algodres granite are prismatic and elongated, and a minority have acicular shape. The zircon rims (6–20 μ m) are narrow and some of them have an incipient oscillatory zoning in the core (Fig. 3e). A large proportion of the zircon have 101 pyramids and 100 prisms. The Th/U ratio exhibits a large range of values, from 0.02 to 7.1.

Thirty-three zircons were analyzed, resulting in 26 grains with younger dates. From the 26 younger dates, 20 of them defines a cluster of absolute dates between 307 and 320 Ma (Table 1), similar within error between them, whose weighted mean average date is 312.9 ± 1.6 (MSWD = 1.6) (Fig. 4e) which is considered the crystallization age of the X γ granite. Three concordant older zircon grains provide Neoproterozoic dates from 600 to 750 Ma (Table 2).

Inherited zircon

A general overview of the inherited zircon grains found in the granites (total of 40 concordant ages) allowed to ascribe them to different age groups: 400–500 Ma, 500–650 Ma, 650–850 Ma and 2000–2500 Ma (Table 2). These age distributions help us constraining possible protoliths as the source of the FCR–LAC granites.

Apatite U–Pb ages

In general, the apatite grains appear as elongated prisms, but occasionally show anhedral rounded shapes. Regarding the texture, the apatite grains do not show oscillatory zoning at backscattered electron imaging. However, the BSE imaging revealed several very small zircon inclusions (Fig. 5). Apatite ages analyses (Table 3) are plotted in the Tera–Wasserburg (TW) diagrams due to their high and variable common Pb (Pb_{cm})/radiogenic Pb ratios, precluding further Pb_{cm} corrections. The TW regression results in the determination of the initial Pb_{cm} composition and cooling age.

Regarding the number of analyzed grains, around 25 apatite grains per granite were targeted, and apatite ages were

estimated from ca. 22 grains. All these grains fall on an isochron in the TW diagram supporting the idea that they are cogenetic despite their rounded morphologies.

For the five granitic facies mentioned above, the following TW Concordia lower-intercept apatite ages were obtained: II γ (301.4 ± 2.6 Ma; MSWD = 0.8), III γ (288.0 ± 14.0 Ma; MSWD = 3.3), V γ (306.6 ± 8.5 Ma; MSWD = 3.9), IX γ (307.0 ± 10.0 Ma; MSWD = 3.6), and X γ (302.6 ± 5.6 Ma; MSWD = 1.9) (Fig. 6). The apatite ages reflect the timing at which the apatite closure temperature (450–550 °C; Schoene and Bowring 2007) was reached after their crystallization and are, therefore, younger than the equivalent magmatic zircon ages.

Discussion

Th/U zircon ratios in S-type granites

Th/U ratios have long been considered as an effective discriminator between metamorphic and magmatic zircon, with the value of 0.1 being a threshold below and above which, respectively, are placed those two types of zircons (e.g., Williams et al. 1996; Rubatto and Gebauer 2000). However, it has been demonstrated that Th/U ratios can not be used as a rule of thumb given that the Th/U ratio of zircon largely depends on the coexistence with Th-rich minerals such as monazite and allanite (Möller et al. 2003; Schaltegger and Davies 2017). For example, Rubatto (2017) showed that the occurrence of high-grade metamorphic rocks with zircons depicting Th/U > 0.1 is not rare, while Yakymchuk et al. (2018) referred a population of metamorphic zircons from Western Australia having a mean Th/U ratio of 0.4. On the other hand, Lopez-Sanchez et al. (2016) reported Th/U < 0.1 for zircon overgrowths of magmatic origin.

Considering all these facts, the reported Th/U ratios (Table 1) might be considered with caution. Indeed, due to the petrogenetic nature of these granites, with the melt being segregated from a HT metamorphic rock, it is expectable that magmatic zircon shows variable Th/U ratios. Under these circumstances, the determined zircon Th/U ratios can not be used as an independent discriminant factor for magmatic vs. metamorphic origin.

The timing of granites emplacement

The FCR–LAC granites have different facies allowing their subdivision in 10 distinct granitic bodies, referred as I γ to X γ , from oldest to young, based on the geometries of their contacts (Ribeiro 2001).

In this study, we obtained U–Pb zircon ages for the five most representative granite facies, (II γ , III γ , V γ , IX γ and X γ). Many of our ages are identical within error, despite

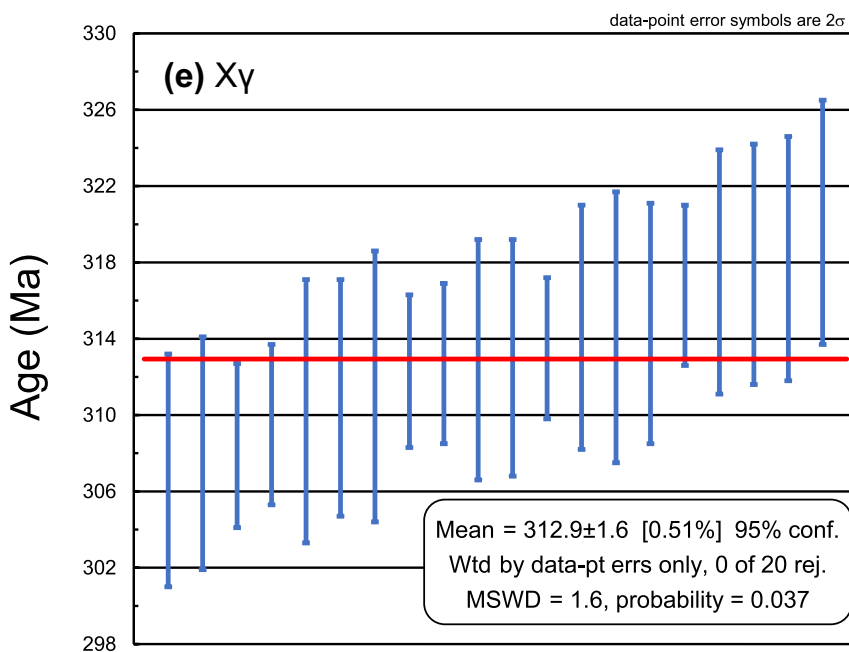
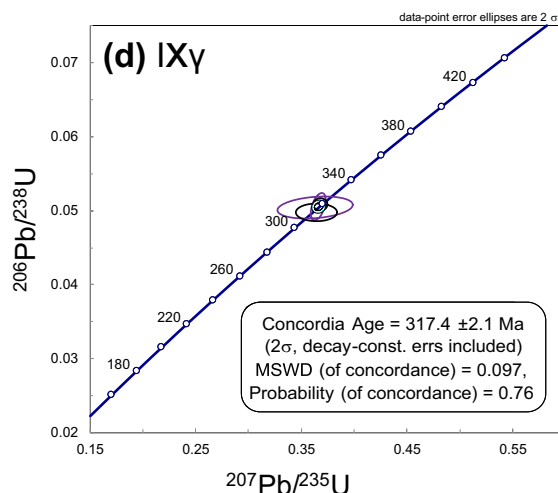
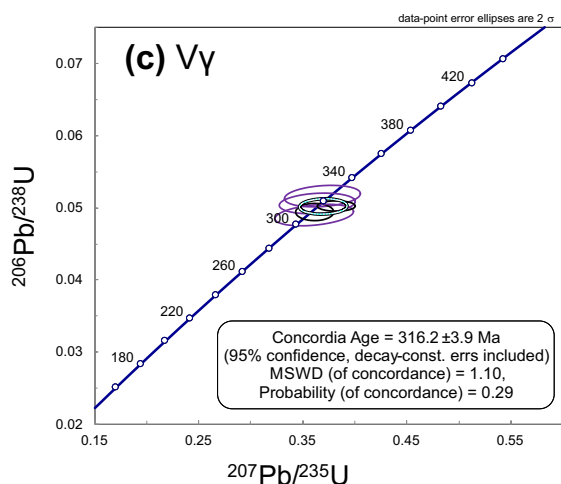
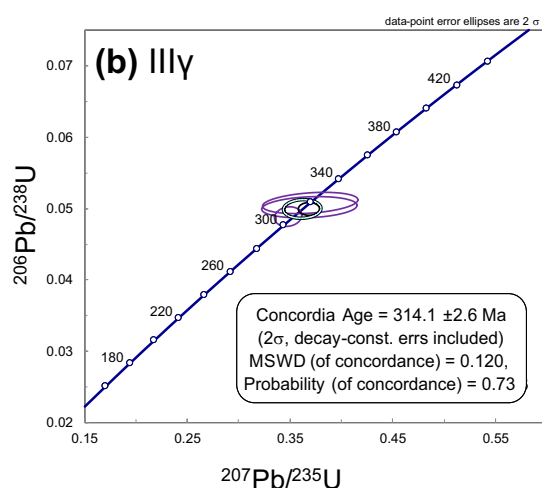
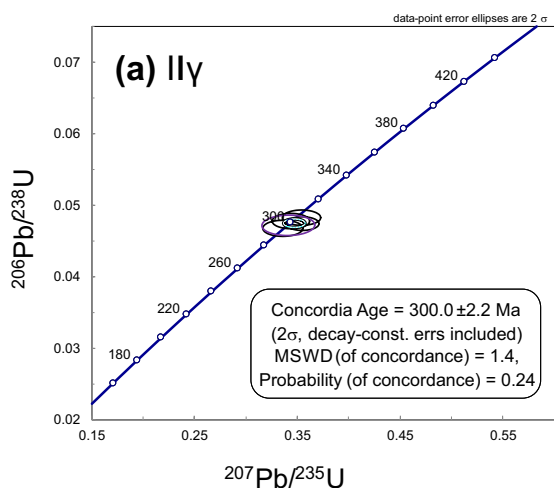


Fig. 4 Wetherill concordia diagrams showing the U–Pb crystallization ages for: **a** São Pedro-Vieiro granite (II γ); **b** Ribeira de Massueime-Galegos granite (III γ); **c** Chãs-Amargo granite (V γ); **d** Méda-Escalhão granite (IX γ). **e** U–Pb crystallization ages of Sta. Comba-Algodres granite (X γ) are represented by a weighted mean average diagram

ages spanning from 300.0 ± 2.2 Ma (II γ) to 317 ± 2.1 Ma (IX γ). In the light of these new results, our data indicate that the FCR–LAC granite suite crystallized between 317 and 313 Ma with the final emplacement of II γ at ca. 300 Ma, supported by its intrusive field relationships with respect to the anatectic complex (Fig. 4).

It must be emphasized that the complexity of this granitic region can be higher than it can be inferred from the 10 mapped facies. Indeed, for the II γ granite, besides the age here presented (300.0 ± 2.2 Ma), another age has been obtained, with similar number of zircons used to infer a concordia age, yielding 307.8 ± 3.1 Ma (Díez Fernández and Pereira 2017). This suggests that the II γ granite can comprise more than one late intrusive body, but reinforces it being a late magmatic episode affecting this region. The crystallization age of the II γ granite is substantially younger than the age obtained by Macedo (1988) of 319 ± 6 Ma using the K–Ar dating method. However, K–Ar ages are known to be prone to the effects of post-magmatic alteration processes leading commonly to younger ages by Ar loss (e.g. Baksi 1994), but also to older ages as a consequence of preferential K mobility (e.g., Cerling et al. 1985). Indeed, these authors demonstrated that low-temperature alteration involving meteoric water can result in hydrogen exchange by K^+ and Na^+ without significant alteration of other elements, conditions under which Ar also appears to be less mobile than alkali ions. Also, Mata et al. (2015) noticed that dates determined by the K–Ar method elsewhere for doleritic rocks portraying evidences for alteration, resulted in older dates than those obtained by more robust methods.

The obtained age for II γ granite confirms the diachronous deformation along this shear zone, progressing from east (Juzbado) to west (Penalva do Castelo), as previously suggested by Pereira et al. (2017). Indeed, in Juzbado, the eastern sector of the JPCSZ, the last shear event has been dated at 309 ± 2.5 Ma (^{40}Ar – ^{39}Ar in white micas; Gutiérrez-Alonso et al. 2015). Later, Valle Aguado et al. (2017) showed that in the western sector deformation continued until ca. 299 Ma, which is within error of the date, we obtained for the D₃-affected II γ granite (300.0 ± 2.2 Ma).

In the CIZ, significant granitic plutonism has been considered to occur during syn-, late- and post-D₃ stage (e.g., Ferreira et al. 1987; Azevedo and Valle Aguado 2013). Particularly, granites from this studied region have been classified as syn-D₃ which has been mainly developed between 310 and 320 Ma (e.g. Ribeiro 2001; Azevedo and Valle

Aguado 2013). However, as mentioned before, II γ granite (300.0 ± 2.2 Ma) was clearly deformed by D₃ allowing to consider it as late-D₃, while the other dated facies are syn-D₃.

Protoliths of the granites

The obtained data for inherited zircon data were compared with published detrital zircon ages from distinct domains of the Douro-Beiras Supergroup in the CIZ, namely the metasediments from the Northern and Southern domains (Orejana et al. 2015). Comparison with the kernel density estimate (KDE) plots for these domains (Fig. 7) puts in evidence the similarities between metasediments of the Northern domain with our data, namely the existence of a main age group of the Lower Cambrian/Cryogenian, with minor Tonian and Paleoproterozoic contributions, and the absence of Mesoproterozoic ages.

Moreover, the second representative group of ages, 400–500 Ma (Upper Cambrian/Lower Devonian), seems to be related with the Ollo de Sapo formation that was emplaced in the Iberian Massif between 495 and 470 Ma (García-Arias et al. 2018). These ages suggest that the Douro-Beiras Supergroup metasediments that melted to form these granites also included Ollo de Sapo magmatic rocks.

Cooling and exhumation rates

In this work, we determined U–Pb ages for zircon and apatite occurring in the same rocks (see above), providing an opportunity to assess the cooling history of the granitic rocks where they crystallized. Indeed, closure temperatures (T_c) for the system U–Pb are usually considered to be in excess of 900 °C for zircon (Cherniak and Watson 2000), while for apatite T_c of 450–550 °C has been usually considered (Schoene and Bowring 2007). However, there have been reported apatite closure temperatures above 800 °C in doleritic rocks from the Armorican Massif (Pochon et al. 2016).

The concept of closure temperature was proposed by Dodson (1973) as referring to the temperature of a mineral at the time of its apparent (“freezing”) age. It can be determined from:

$$E/RT_c = \ln \left[-AD_0RT_c^2 / \{a^2(dT/dt)E\} \right],$$

where E is the activation energy for the diffusion process, R is the ideal gas constant, T_c is the closure temperature, A is a numerical constant depending on the geometry of the grain (spherical or cylindrical), D_0 is the diffusion coefficient at infinitely high temperature, dT/dt is the cooling rate and a is an effective diffusion dimension (i.e., radius in the case of a sphere). This approach has implicit the role of the daughter element volume diffusion over time, which is

Table 2 LA-ICP-MS U–Pb inherited zircon data of the Figueira de Castelo Rodrigo–Lumbreres anatectic complex granites

Id	U (ppm)		Th (ppm)	Th/U	Common-lead uncorrected		Final ages (Ma)		$^{206}\text{Pb}/^{238}\text{U}$	$\pm 2\sigma$	$^{207}\text{Pb}/^{235}\text{U}$	$\pm 2\sigma$	$^{207}\text{Pb}/^{206}\text{Pb}$	$\pm 2\sigma$	Concordance (%) ^b	
					$^{207}\text{Pb}/^{235}\text{U}$	$\pm 2\sigma$	$^{206}\text{Pb}/^{238}\text{U}$	$\pm 2\sigma$								Rho ^a
São Pedro-Vieiro granite (IIγ)																
M7_36_2c	537	28	0.05	0.05	0.531	0.023	0.0692	0.0019	0.002	429	15	431	11	409	70	100
M7_36_19c	552	126	0.23	0.23	0.589	0.021	0.0744	0.0013	0.001	469	14	463	8	474	71	99
M7_36_9c	282	106	0.38	0.38	0.573	0.023	0.0752	0.0013	0.001	458	15	468	8	385	80	102
M7_36_15c	690	344	0.50	0.50	0.602	0.021	0.0772	0.0014	0.001	477	13	479	8	452	69	100
M7_36_12c	578	158	0.27	0.27	0.659	0.023	0.0806	0.0013	0.001	512	14	500	8	547	69	98
M7_36_13c	1060	297	0.28	0.28	0.698	0.023	0.0866	0.0014	0.001	537	14	536	8	537	62	100
M7_36_1c	310	250	0.81	0.81	0.718	0.027	0.0901	0.0016	0.002	548	16	556	9	494	75	102
M7_36_14c	455	316	0.69	0.69	0.77	0.028	0.0908	0.0016	0.002	578	16	560	10	635	71	97
M7_36_8c	504	314	0.62	0.62	0.751	0.026	0.0913	0.0016	0.002	568	15	564	10	574	64	99
M7_36_10c	317	128	0.40	0.40	0.82	0.031	0.0999	0.0017	0.002	605	17	614	10	552	73	101
M7_36_14e	146	90	0.62	0.62	6.25	0.19	0.3821	0.0099	0.43	1997	26	2082	46	1907	54	109
Ribeira de Massueime-Galegos granite (IIγ)																
M7_13_11e	365	66	0.18	0.18	0.582	0.032	0.0782	0.0024	0.28	457	20	485	14	370	110	106
M7_13_6c	336	101	0.30	0.30	0.725	0.027	0.0861	0.0015	0.002	553	16	532	9	612	74	96
M7_13_7c	1101	314	0.28	0.28	0.71	0.023	0.0872	0.0014	0.001	544	14	539	8	553	60	99
M7_13_12c	469	250	0.53	0.53	0.716	0.026	0.0884	0.0015	0.002	547	15	546	9	531	70	100
M5_13_4	690	512	0.74	0.74	0.853	0.085	0.0997	0.0024	0.002	623	46	613	14	605	180	98
Chãs-Amargo granite (Vγ)																
M6_12_18e	647	1	0.002	0.002	0.512	0.042	0.0656	0.0016	0.11	417	28	409	10	424	180	98
M6_12_15e	412	84	0.20	0.20	0.479	0.044	0.0669	0.0023	0.42	398	32	417	14	265	190	105
M6_12_20e	1199	177	0.15	0.15	0.5	0.04	0.0669	0.0016	0.19	414	27	418	10	366	170	101
M6_12_5e	1043	132	0.13	0.13	0.507	0.041	0.0678	0.0017	0.35	415	28	423	10	346	180	102
M6_12_15c	457	35	0.08	0.08	0.567	0.027	0.0714	0.0015	0.002	456	17	444	9	472	110	98
M1_12_8	263	256	0.97	0.97	0.666	0.031	0.0843	0.0012	0.001	516	20	522	7	486	94	101
M1_12_1a	556	226	0.41	0.41	0.755	0.032	0.0925	0.0012	0.001	569	19	570	7	485	82	100
M1_12_7	97	84	0.87	0.87	0.76	0.045	0.0928	0.0017	0.002	566	26	572	10	510	120	101
M6_12_21e	788	213	0.27	0.27	0.821	0.066	0.0953	0.0023	0.30	605	36	587	13	656	170	97
M1_12_2	150	142	0.95	0.95	0.808	0.044	0.0971	0.0015	0.002	593	25	597	9	496	110	101
M6_12_11c	335	282	0.84	0.84	0.798	0.037	0.098	0.002	0.002	594	21	600	12	542	100	101
M6_12_19c	527	336	0.64	0.64	0.82	0.036	0.098	0.002	0.002	607	21	603	12	600	100	99
M6_12_23c	1653	130	0.08	0.08	0.832	0.034	0.099	0.002	0.002	614	19	606	12	634	92	99
M6_12_17c	186	104	0.56	0.56	0.837	0.041	0.1015	0.0023	0.002	616	23	623	13	550	110	101
M6_12_16c	342	129	0.38	0.38	1.232	0.054	0.1349	0.0028	0.003	814	24	815	16	784	94	100

Table 2 (continued)

Id	U (ppm)	Th (ppm)	Th/U	Common-lead uncorrected		Final ages (Ma)		Concordance (%) ^b						
				²⁰⁷ Pb/ ²³⁵ U ± 2σ	²⁰⁶ Pb/ ²³⁸ U ± 2σ	²⁰⁷ Pb/ ²³⁵ U ± 2σ	²⁰⁶ Pb/ ²³⁸ U ± 2σ							
M6_12_14c	162	112	0.69	12.35	0.52	0.4769	0.0098	0.010	2629	43	2512	2704	71	93
Média-Escalhão granite (IXγ)														
M6_45_6e	1385	2	0.001	0.609	0.048	0.0766	0.0017	0.22	481	10	476	479	170	99
M4_45_8a	611	169	0.28	0.766	0.029	0.094	0.003	0.003	572	17	578	521	79	101
M4_45_1	162	55	0.34	0.796	0.024	0.097	0.0016	0.002	592	9	596	561	64	101
M4_45_3	221	113	0.51	0.891	0.024	0.1057	0.0016	0.002	643	9	648	599	59	101
M4_45_5	151	75	0.50	1.015	0.062	0.1249	0.0042	0.004	692	24	758	450	130	110
Sta. Comba-Algodres granite (Xγ)														
M6_34_8c	238	129	0.54	0.813	0.039	0.0976	0.0021	0.002	601	12	600	564	100	100
M6_34_12c	263	389	1.48	0.926	0.039	0.1061	0.0017	0.02	654	10	650	609	95	99
M6_34_29c	73	36	0.49	1.03	0.06	0.1197	0.0029	0.003	713	17	728	613	130	102

^aRho is calculated by Iolite package software and it corresponds to the correlation between the given errors of the ²⁰⁷Pb/²³⁵U and ²⁰⁶Pb/²³⁸U ratios
^aConcordance = (²⁰⁶Pb/²³⁸U age) / (²⁰⁷Pb/²³⁵U age) × 100 – for ages < 900 Ma = (²⁰⁶Pb/²³⁸U age) / (²⁰⁷Pb/²³⁵U age) × 100 – for ages > 900 Ma

function of temperature. Moreover, the T_c is also dependent on the cooling rate. The T_c parameter appears on both sides of equation, so the equation is solved through several iterations for a given value of cooling rate. This procedure allows to calculate a consistent set of closure temperatures and cooling rates from the ages of two mineral species. For these calculations, the zircon and apatite diffusion parameters compiled by Hodges et al. (2003) were used.

Ti-in-zircon and the zircon saturation ($T_{Zircsat}$) geothermometers were determined in this study. The Ti-in-zircon geothermometer uses the Ti content in the zircon structure, which is dependent on temperature and independent of pressure, to estimate the magma temperature at the time of zircon crystallisation (Watson et al. 2006). The $T_{Zircsat}$ predicts the temperature at which zircon crystallisation begins in a cooling magma, and, on the other hand, the temperatures above which zircon dissolution should occur (Watson and Harrison 1983).

In the case of zircon, we were faced with the problem that the experimental closure temperature (> 900 °C; Cherniak and Watson 2000) is clearly above of those determined by Ti-in-zircon and $T_{Zircsat}$ geothermometers (Table 4), indicating that the studied zircon grains grew below their closure temperatures and, consequently, that diffusion processes did not occur after crystallization. Recently, Siégl et al. (2018) have shown that $T_{Zircsat}$ is a dynamic variable that changes during magma crystallisation, and, thus, can not be used to constrain magmatic or partial melting temperatures. Consequently, we used the Ti-in-zircon geothermometer (Watson et al. 2006), which is considered as providing very reliable zircon crystallization temperatures, and therefore used as zircon closure temperatures. For the granite facies Vγ, IXγ and Xγ the use of this thermometer led to the following crystallization temperatures: Vγ = 825 ± 22 °C, IXγ = 836 ± 22 °C, and Xγ = 783 ± 31 °C (Table 4).

The obtained temperatures are endorsed by data published by Pereira et al. (2017) pointing to metamorphic temperatures in excess of 800 °C at the onset of partial melting. These results are also consistent with extensive literature on the melting of pelitic rocks to form anatectic granitoids (e.g. Clemens 2003; Bento dos Santos et al. 2011; Clemens and Stevens 2016).

The next step was to obtain the apatite closure temperature for each granite facies through Dodson’s equation, using $T_c = 446$ °C as an initial experimental value, as proposed by Cherniak et al. (1991). This provided T_c results between 483 and 465 °C (Table 5).

Combining the zircon and apatite T_c with their respective ages, the cooling rates for the IIIγ, Vγ, IXγ and Xγ granite facies are of 13, 34, 35 and 28 °C Ma⁻¹, respectively (Table 5). It was not possible to infer the closure temperatures and respective cooling rates for the IIγ

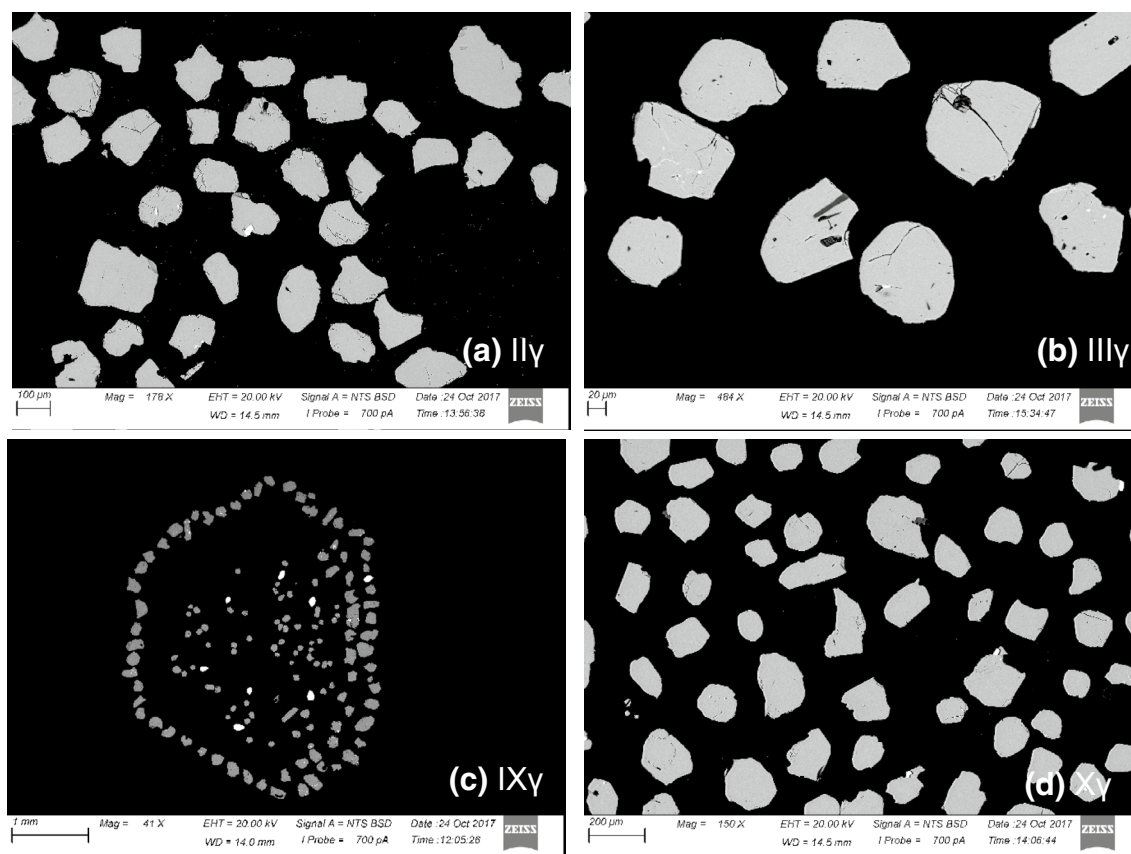


Fig. 5 Back-scattered electron images of representative apatite grains of four studied granites: **a** São Pedro-Vieiro granite (II γ); **b** Ribeira de Massueime-Galegos granite (III γ); **c** Mêda-Escalhão granite (IX γ); **d** Sta. Comba-Algodres granite (X γ)

granite, because the apatite ages are slightly older than the zircon ages obtained for this sample, even considering their errors.

Cooling rates of plutons are highly variable, with published values differing by more than two orders of magnitude (e.g. Chesley et al. 1993; Tsuchiya and Fujino 2000; Meert et al. 2001; Miyazaki and Santosh 2005). It depends essentially on the way heat is exchanged between the hot intrusive body and their surroundings. The heat transfer may be done by conduction or by fluid-assisted advection. Considering that thermal diffusivity is strongly dependent on temperature, with which correlates negatively, and the role of the latent heat of crystallization on lowering the cooling rate of a crystallizing melt (Whittington et al. 2009; Nabelek et al. 2012), the rates of conductive cooling are very low when compared with advective cooling.

Although it was not possible to infer the cooling rate for the II γ granite, the closeness of the zircon and apatite crystallization ages points to an abrupt cooling, at least until the apatite T_c . This suggests the localized intervention of significant fluid circulation during cooling within the JPCSZ. This hypothesis receives some support from the occurrence of abundant tourmaline in the diatexites and significant iron

oxides enrichment in the metasedimentary rocks in contact with this granite facies.

The estimated granite cooling rates are similar for V γ and IX γ , (34 ± 4.1 and 35 ± 3.1 °C Ma⁻¹) and lower for III γ and X γ granite concerning their absolute value (13 ± 16.5 and 28 ± 39.5 °C Ma⁻¹). Nonetheless, these cooling rates are all identical within error. Comparing these cooling rates, particularly the V γ and IX γ granites yielding small uncertainties, with high temperature metamorphic complexes (Spear and Parrish 1996; Bento dos Santos et al. 2010, 2014), allows us to infer fast cooling conditions. In geodynamic settings where granitoid cooling is mainly driven by denudation, cooling rates are substantially lower, typically spanning from 0.5 to 5 °C Ma⁻¹ (Ashwal et al. 1999; Munhá et al. 2005; Gallien et al. 2010; Bento dos Santos et al. 2010, 2014; Scibiowski et al. 2015). Cooling rates of the FCR–LAC granites are, therefore, compatible with rapid exhumation mechanisms and shallow crustal emplacement.

Gravity has been considered an important constrainer during the late stages of the collisional orogens, when the tectonic driving orogenic forces diminishes or ceases its influence (Jadamec et al. 2007). This leads to lateral release of potential gravitational energy characterizing the thickened

Table 3 LA-ICP-MS U–Pb apatite data of the Figueira de Castelo Rodrigo–Lumbrals anatectic complex granites

Id	U (ppm)	Pb (ppm)	$^{206}\text{Pb}_{\text{cm}}$	$^{238}\text{U}/^{206}\text{Pb}$	$\pm 2\sigma$	$^{207}\text{Pb}/^{206}\text{Pb}$	$\pm 2\sigma$	Rho ^b	Final ages (Ma) ^b			
									$^{207}\text{Pb}/^{235}\text{U}$	$\pm 2\sigma$	$^{206}\text{Pb}/^{238}\text{U}$	$\pm 2\sigma$
São Pedro-Vieiro granite (II γ)												
M4_36_1	111	10	0.36	13.4	0.29	0.3393	0.0029	0.56	1523	17	464	10
M4_36_10	299	11	0.18	16.98	0.37	0.1991	0.0021	0.46	978	15	369	8
M4_36_2	99	10	0.38	13.22	0.30	0.3572	0.0048	0.32	1574	20	470	10
M4_36_3	246	10	0.19	16.96	0.37	0.2073	0.0018	0.31	1002	14	369	8
M4_36_4	79	12	0.50	11.13	0.26	0.4357	0.0052	0.54	1879	20	554	12
M4_36_5	51	9	0.54	10.18	0.23	0.472	0.005	0.63	2029	20	604	13
M4_36_6	359	13	0.18	17.32	0.36	0.195	0.0012	0.40	951	13	362	8
M4_36_7	311	11	0.16	17.39	0.36	0.1892	0.0014	0.32	930	13	361	8
M4_36_8	262	13	0.23	16.19	0.34	0.2352	0.0016	0.43	1116	15	386	8
M4_36_9	65	9	0.48	11.15	0.25	0.4212	0.0045	0.37	1852	20	554	12
M4_36_11	116	11	0.25	15.45	0.24	0.2587	0.0024	0.38	1213	12	404	6
M4_36_12	181	10	0.22	16.36	0.25	0.2267	0.0021	0.32	1084	11	383	6
M4_36_13	88	9	0.51	9.94	0.16	0.4691	0.0056	0.51	2043	15	618	10
M4_36_14	225	12	0.64	7.91	0.13	0.5522	0.0072	0.53	2395	17	767	12
M4_36_16	293	13	0.19	17.14	0.26	0.1979	0.0016	0.32	967	10	366	5
M4_36_17	54	10	0.22	16.36	0.25	0.222	0.002	0.29	1068	11	382	6
M4_36_18	42	11	0.35	13.63	0.20	0.3369	0.0032	0.54	1505	13	456	7
M4_36_19	317	11	0.39	12.48	0.19	0.3743	0.0032	0.51	1660	13	497	7
M4_36_20	295	13	0.38	12.23	0.19	0.3763	0.0037	0.54	1680	14	507	8
Ribeira de Massueime-Galegos granite (III γ)												
M5_13_1	62	10	0.19	10.55	0.23	0.4309	0.0072	0.58	1919	19	584	12
M5_13_2	59	9	0.20	10.85	0.24	0.431	0.009	0.60	1893	19	568	12
M5_13_3	61	12	0.22	9.05	0.20	0.4806	0.0094	0.21	2150	22	675	15
M5_13_4	36	12	0.25	7.09	0.16	0.5756	0.0102	0.56	2536	20	851	18
M5_13_5	70	9	0.17	11.49	0.25	0.4034	0.0066	0.40	1792	19	538	11
M5_13_6	48	12	0.23	8.48	0.19	0.52	0.01	0.53	2281	20	719	15
M5_13_8	61	9	0.18	10.64	0.27	0.4409	0.0152	0.53	1930	22	579	14
M5_13_9	89	11	0.17	11.64	0.26	0.3950	0.0062	0.49	1762	18	531	11
M5_13_12	87	11	0.16	12.53	0.20	0.3827	0.0076	0.19	1674	15	495	8
M5_13_13	78	10	0.14	14.03	0.22	0.326	0.007	0.42	1458	13	444	7
M5_13_14	67	10	0.26	8.01	0.15	0.558	0.0132	0.09	2393	20	759	13
M5_13_15	497	100	0.15	13.56	0.22	0.3492	0.0064	0.39	1536	13	459	7
M5_13_16	75	11	0.16	13.72	0.23	0.3542	0.0098	0.39	1536	15	454	7
M5_13_17	80	10	0.14	13.59	0.31	0.3518	0.0186	−0.60	1530	34	458	10
M5_13_20	61	9	0.20	10.46	0.18	0.4589	0.0116	0.61	1979	15	588	10
Chãs-Amargo granite (V γ)												
M1_12_1	98	20	0.55	9.42	0.20	0.4846	0.0029	0.54	2121	19	650	13
M1_12_10	92	10	0.40	12.41	0.28	0.372	0.0037	−0.06	1659	20	500	11
M1_12_2	94	11	0.38	12.47	0.26	0.361	0.003	0.50	1630	18	497	10
M1_12_3	106	15	0.49	11.58	0.25	0.445	0.004	0.55	1869	19	534	12
M1_12_4	176	15	0.33	13.78	0.28	0.3137	0.0019	0.40	1442	17	452	9
M1_12_5	155	13	0.31	13.87	0.29	0.3076	0.0022	0.33	1421	17	449	9
M1_12_6	95	19	0.54	9.38	0.20	0.4878	0.0031	0.40	2132	19	653	13
M1_12_7	95	18	0.53	9.6	0.20	0.4811	0.0029	0.36	2097	19	639	13
M1_12_8	69	7	0.36	12.86	0.28	0.3544	0.0031	0.49	1592	18	483	10
M1_12_9	59	13	0.58	9.0	0.20	0.4985	0.0041	0.10	2188	21	679	14
M1_12_11	89	20	0.55	8.78	0.20	0.5123	0.0048	0.57	2233	21	695	15

Table 3 (continued)

Id	U (ppm)	Pb (ppm)	$^{206}\text{Pb}_{\text{cm}}$	$^{238}\text{U}/^{206}\text{Pb}$	$\pm 2\sigma$	$^{207}\text{Pb}/^{206}\text{Pb}$	$\pm 2\sigma$	Rho ^b	Final ages (Ma) ^b			
									$^{207}\text{Pb}/^{235}\text{U}$	$\pm 2\sigma$	$^{206}\text{Pb}/^{238}\text{U}$	$\pm 2\sigma$
M1_12_12	84	16	0.52	9.62	0.22	0.4794	0.0053	0.47	2095	21	639	15
M1_12_13	98	11	0.40	12.37	0.29	0.3652	0.0041	0.32	1647	20	501	11
M1_12_14	12	23	0.94	1.62	0.04	0.781	0.0082	0.21	4277	26	3104	61
M1_12_15	85	15	0.51	9.94	0.23	0.4665	0.0047	0.50	2039	21	618	14
M1_12_16	80	12	0.50	10.5	0.24	0.4421	0.0043	0.53	1944	20	586	13
M1_12_17	90	12	0.45	11.16	0.25	0.413	0.004	0.61	1834	20	553	12
M1_12_18	94	14	0.46	10.7	0.24	0.4301	0.0038	0.46	1906	20	576	13
M1_12_19	130	18	0.45	10.94	0.29	0.401	0.005	-0.22	1824	26	564	14
M1_12_20	90	12	0.42	11.38	0.26	0.3918	0.0039	0.56	1773	20	543	12
M1_12_21	99	17	0.43	10.05	0.27	0.463	0.008	0.56	2018	24	611	16
M1_12_22	85	24	0.57	7.63	0.20	0.557	0.0082	0.55	2436	25	794	20
M1_12_23	97	15	0.42	10.42	0.28	0.4501	0.0075	0.31	1959	25	591	15
M1_12_24	83	15	0.47	9.77	0.27	0.485	0.008	0.58	2082	25	628	16
M1_12_25	84	15	0.64	9.98	0.29	0.4779	0.0092	0.57	2049	26	615	17
Mêda-Escalhão granite (IXγ)												
M4_45_1	141	11	0.32	13.92	0.29	0.3122	0.0024	0.39	1429	17	447	9
M4_45_10	141	16	0.41	12.44	0.26	0.376	0.0022	0.40	1668	18	498	10
M4_45_2	114	15	0.41	11.75	0.25	0.4012	0.0027	0.54	1767	18	527	11
M4_45_3	139	12	0.34	13.54	0.29	0.325	0.0024	0.55	1481	17	459	10
M4_45_4	140	18	0.43	11.87	0.25	0.3946	0.0024	0.48	1746	18	522	11
M4_45_5	138	14	0.37	12.68	0.27	0.356	0.0024	0.43	1606	18	489	10
M4_45_6	138	18	0.42	11.72	0.25	0.3958	0.0022	0.58	1759	18	528	11
M4_45_7	115	15	0.42	11.75	0.25	0.3977	0.0027	0.55	1760	18	526	11
M4_45_8	146	15	0.36	12.79	0.28	0.3564	0.0027	0.41	1600	18	485	10
M4_45_9	136	14	0.39	12.88	0.28	0.356	0.0025	0.26	1594	18	482	10
M4_45_11	159	14	0.44	11.67	0.18	0.4123	0.0036	0.56	1796	13	530	8
M4_45_14	126	17	0.40	11.66	0.18	0.3791	0.0035	0.51	1725	14	530	8
M4_45_15	128	15	0.67	6.49	0.13	0.6188	0.0075	0.08	2684	21	924	17
M4_45_16	33	12	0.40	12.6	0.19	0.3699	0.0036	0.51	1641	13	492	7
M4_45_18	135	13	0.34	13.25	0.21	0.35	0.0036	0.51	1558	13	469	7
M4_45_19	282	18	0.25	15.08	0.23	0.2729	0.0023	0.51	1269	11	414	6
M4_45_20	130	14	0.41	12.58	0.19	0.374	0.0034	0.53	1653	13	493	7
M4_45_21	153	15	0.39	13.07	0.34	0.3421	0.0054	0.57	1545	22	475	12
M4_45_22	55	8	0.62	10.88	0.32	0.431	0.011	0.45	1884	28	567	16
M4_45_23	123	19	0.49	10.17	0.28	0.4232	0.0067	0.46	1930	25	604	16
M4_45_24	149	15	0.40	12.7	0.34	0.3512	0.0052	0.49	1589	22	488	13
M4_45_25	138	16	0.38	12.11	0.32	0.3784	0.0054	0.41	1690	23	511	13
Sta. Comba-Algodres granite (Xγ)												
M4_34_1	38.24	8.359	0.57	9.08	0.20	0.5113	0.0057	0.57	2201	20	673	14
M4_34_10	44.61	8.646	0.53	9.62	0.21	0.4816	0.0047	0.51	2097	20	638	14
M4_34_2	35.45	8.788	0.60	8.36	0.18	0.5302	0.0055	0.57	2308	20	728	15
M4_34_3	53.08	8.5	0.46	10.63	0.24	0.4365	0.0043	0.70	1924	19	580	12
M4_34_4	54.59	8.46	0.45	10.7	0.24	0.4217	0.0041	0.46	1890	19	576	12
M4_34_5	57.54	8.24	0.48	11.24	0.24	0.419	0.004	0.51	1839	19	549	11
M4_34_6	54.41	9.529	0.49	10.19	0.22	0.4586	0.0037	0.43	2003	19	603	13
M4_34_7	43.07	8.873	0.55	9.35	0.20	0.4952	0.0047	0.66	2146	20	655	14
M4_34_8	54.15	8.225	0.49	10.89	0.24	0.4298	0.0043	0.50	1889	19	566	12
M4_34_9	48.22	8.475	0.52	10.14	0.23	0.4604	0.0049	0.64	2010	19	606	13

Table 3 (continued)

Id	U (ppm)	Pb (ppm)	$^{206}\text{Pb}_{\text{cm}}$	$^{238}\text{U}/^{206}\text{Pb}$	$\pm 2\sigma$	$^{207}\text{Pb}/^{206}\text{Pb}$	$\pm 2\sigma$	Rho ^b	Final ages (Ma) ^b			
									$^{207}\text{Pb}/^{235}\text{U}$	$\pm 2\sigma$	$^{206}\text{Pb}/^{238}\text{U}$	$\pm 2\sigma$
M4_34_12	55.07	8.82	0.68	6.86	0.11	0.595	0.006	0.54	2600	16	877	13
M4_34_13	52.78	8.571	0.74	5.63	0.09	0.6467	0.0063	0.59	2864	16	1053	16
M4_34_14	48.76	8.42	0.75	5.56	0.10	0.6421	0.0074	0.57	2869	16	1065	17
M4_34_15	52.77	8.349	0.72	6.62	0.11	0.6046	0.0063	0.55	2649	16	907	14
M4_34_16	45.28	8.54	0.35	13.41	0.22	0.3476	0.0039	0.10	1542	16	464	7
M4_34_17	38.68	9.23	0.26	15.75	0.25	0.259	0.0034	0.06	1202	14	397	6
M4_34_19	51.81	8.844	0.37	12.6	0.21	0.3749	0.0043	0.45	1653	14	492	8
M4_34_20	53.53	8.96	0.24	15.87	0.24	0.2465	0.0024	0.21	1160	12	394	6
M4_34_21	54.86	8.97	0.49	10.5	0.30	0.4455	0.0091	0.60	1940	25	586	16
M4_34_22	39.26	8.8	0.51	8.94	0.26	0.519	0.012	0.57	2214	28	683	19
M4_34_23	40.62	8.34	0.45	9.48	0.28	0.498	0.011	0.56	2127	28	647	19
M4_34_24	54.88	9.63	0.56	10.07	0.28	0.4551	0.0086	0.49	1998	26	610	17

^aRho is calculated by Iolite package software and it corresponds to the correlation between the given errors of the $^{238}\text{U}/^{206}\text{Pb}$ and $^{207}\text{Pb}/^{206}\text{Pb}$ ratios

^b Pb_{cm} not corrected

crust, leading to orogenic collapse (Rey et al. 2001 and references therein). The pressure release associated with such collapse can be viewed as one of the triggering mechanisms for crustal partial melting. Yet, mantle to crust heat transfer and intra-crustal radioactive heating might also be considered as significant mechanisms behind crustal melting (Vanderhaeghe 2009). Independent of the cause, partial melting triggers a significant strength/viscosity and density decrease, promoting the exhumation of migmatitic/granitic complexes, which tend to form domes, emplaced at shallow crustal levels (Vanderhaeghe 2009; Vanderhaeghe et al. 2018). This must be the case of the Tormes dome in the CIZ (Escuder-Viruet et al. 1994).

However, it is not yet clear how fast the exhumation caused by orogenic collapse can be (Vanderhaeghe and Teyssier 2001; Scibiorski et al. 2015). Moreover, the interpretation of the fast cooling rates reported on this study can not be done without taking into account that the anatexitic complex is delimited by high-angle crustal-scale shear zones, which juxtapose side-by-side rocks with clearly distinct metamorphic grades, a structural architecture also evidenced by magnetotelluric imaging (see Fig. 7 in Alves Ribeiro et al. 2017). Granites and the associated high-grade metamorphic rocks preserve a low-dipping non-horizontal transport lineation (6° – 12° ; Pereira et al. 2017), clearly indicative of a significant net vertical mass transfer when the 65–100 km lateral displacement is taken into account. Indeed, the associated migmatites of the FCR–LAC endured a significant tectonic exhumation, corresponding to a combined vertical displacement of 5–8 km (Pereira et al. 2017), which suggest that the granitic rocks within the complex must have endured the same tectonic uplift. Considering the upper Carboniferous geothermal gradient calculated

by Pereira et al. (2017) for the FCR–LAC ($42^{\circ}\text{C km}^{-1}$), and taking into account the estimated closure temperatures and ages for zircon and apatite, the vertical exhumation of granitic rocks would have been, indeed, of ~8 km, thus reinforcing the idea of a common assisted tectonic exhumation for granites and migmatites inside the JPCSZ. Considering these ~8 km vertical exhumation required for the determined cooling rates, exhumation rates of 0.3 – 0.8 mm a^{-1} are obtained. Such exhumation rates are clearly faster than those inferred for erosional denudation of granitic plutons (0.16 mm a^{-1} ; Yuguchi et al. 2017), but similar to granite exhumation rates in strike-slip shear zones (0.6 – 1 mm a^{-1} ; Steenken et al. 2002; Zhang et al. 2004; Annen et al. 2006).

In conclusion, our unprecedented results for cooling and exhumation rates of the FCR–LAC granites clearly support the role of first-order shear zones in assisting the exhumation of mid-crustal rocks as has been described elsewhere (e.g., Steenken et al. 2002; Corsini and Rolland 2009; Schulmann et al. 2008; Bento dos Santos et al. 2010, 2014; Fernández et al. 2013; Díaz-Azpiroz et al. 2014; Pereira et al. 2017), emphasizing the role of the JPCSZ in the emplacement of some Iberian collision-related Variscan granites. This mechanism should also be considered of utmost importance in intracrustal heat transfer, influencing the rheological behavior of the continental crust during and after collisional orogenesis.

Conclusions

The Variscan orogeny dynamics was responsible for the emplacement of several plutono-metamorphic complexes in the Iberian Massif and other sectors of the European

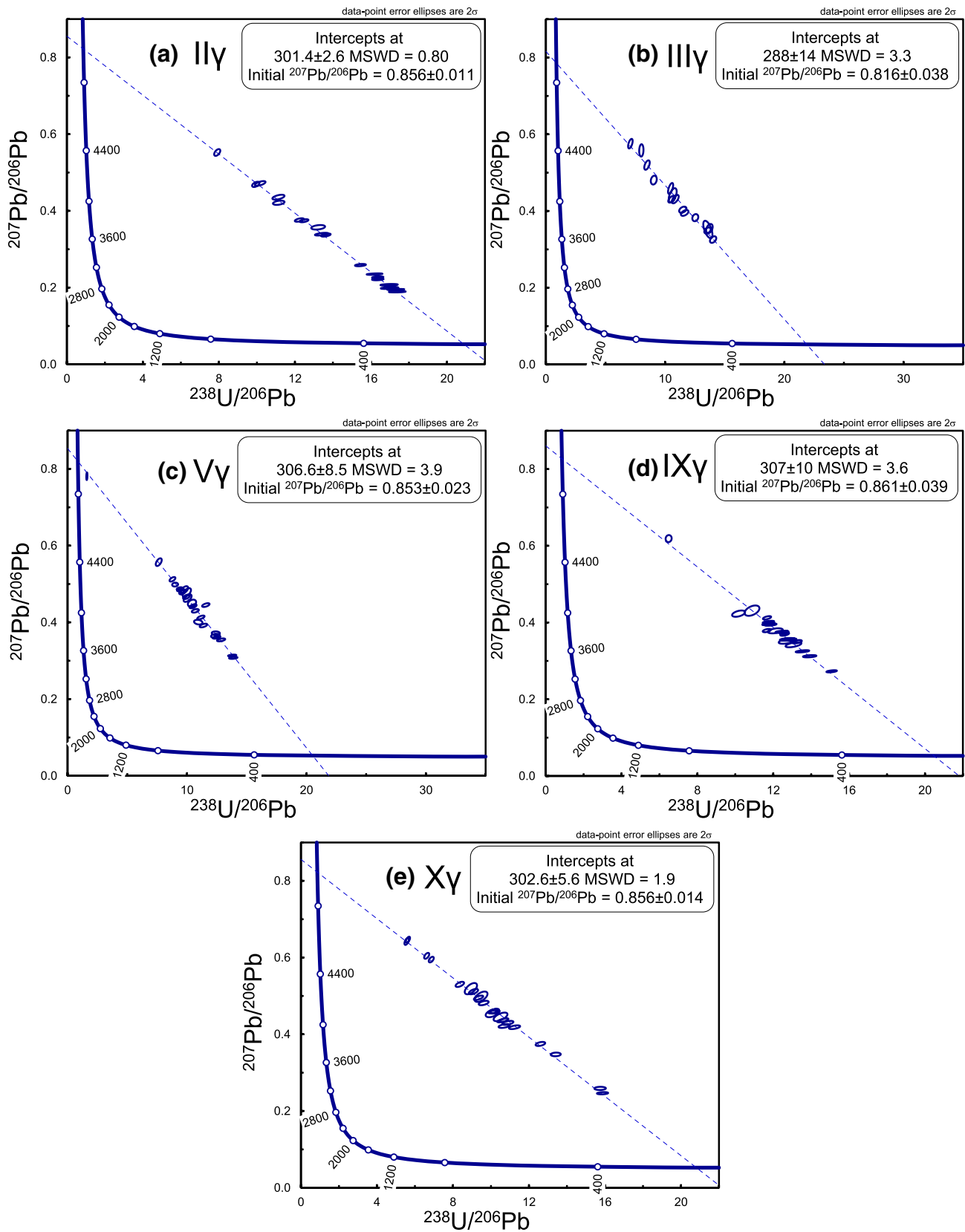


Fig. 6 Tera–Wasserburg U–Pb lower-intercept apatite ages for the five studied granites: **a** São Pedro-Vieiro granite (II γ); **b** Ribeira de Massueime-Galegos granite (III γ); **c** Chãs-Amargo granite (V γ); **d** Mêda-Escalhão granite (IX γ); **e** Sta. Comba-Algodres granite (X γ)

Fig. 7 Kernel density estimates (KDE) plots of inherited zircon ages for the studied granites (a) and also for the detrital zircons of the Northern (b) and Southern domains (c) of the CIZ (Orejana et al. 2015). The defined bin width is 50 Ma. The selected ages to perform the plots are $^{206}\text{Pb}/^{238}\text{U}$, when the age is < 1000 Ma, and $^{207}\text{Pb}/^{206}\text{Pb}$ for ages > 1000 Ma. The KDE plots were performed with the support of the Vermeesch (2018) program (IsoplotR)

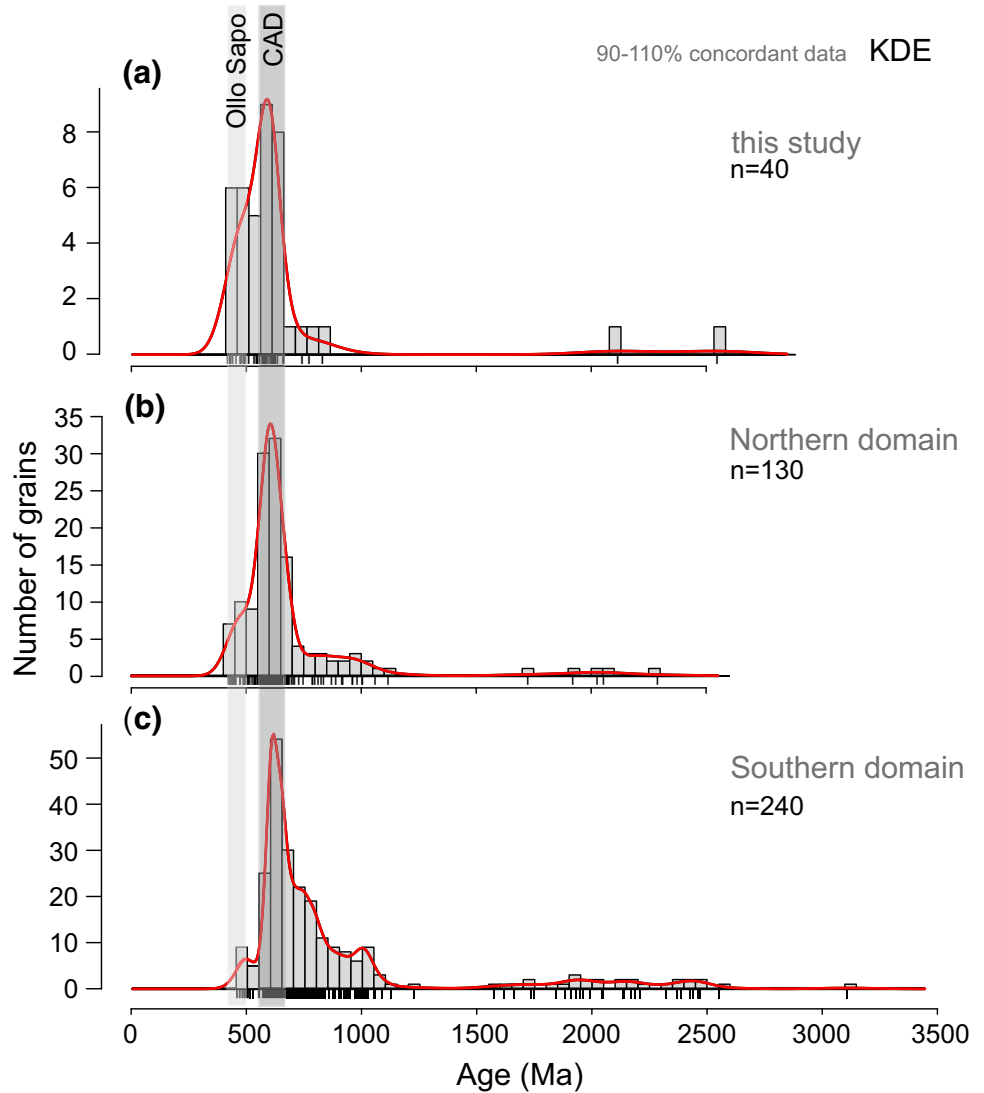


Table 4 Zircon geothermometers applied to the $V\gamma$, $IX\gamma$ and $X\gamma$ granites

Id	Ti-in-zircon thermometer			Zircon saturation thermometer						
	SiO ₂ (wt%)	Ti (ppm)	Error	T (°C)	Zircon	Error	Zr (ppm)	M	Zr. sat lev-els (ppm)	T _{Zircsat} (°C)
$V\gamma$	71.39	24	1.8	825		22	116	1.11	81.9	779
$IX\gamma$	73.6	26.8	1.9	836		22	84	1.12	82.6	751
$X\gamma$	70.97	17.3	2.8	783		31	287	1.22	89.6	854

Variscan Belt. The Figueira de Castelo Rodrigo–Lumbrales Anatectic Complex (FCR–LAC) is an example of a plutono-metamorphic complex where the granite–migmatite association is delimited by two sinistral, east–west to ENE–WSW trending, first-order shear zones (Juzbado–Penalva do Castelo and Huebra shear zones). New U–Pb zircon crystallization ages were determined for 5 different granite facies of this anatectic complex, yielding ages between 300 and 317 Ma, confirming that most of these

granites formed during the syn-D₃ magmatic stage, with the exception of one late-tectonic granite facies which is clearly intrusive into the other facies and yet is affected by the late stages of Variscan shearing. Moreover, since these granites are genetically related with migmatites and both formed and exhumed together, these syn-D₃ crystallization ages (317 ± 2.1–313 ± 1.9 Ma) represent the maximum age (end of D₂ and beginning of D₃) and the duration of anatexis (ca. 5 Ma).

Table 5 Zircon and apatite estimated closure temperatures for the granites in study and the respective cooling and exhumation rates

Id	Zircon age (Ma)	Apatite age (Ma)	Δt (Ma)	Zircon T_c (°C)	Apatite T_c (°C)	Cooling rate (°C Ma ⁻¹)	Exhumation rate (mm a ⁻¹)
II γ	300 ± 2.2	301 ± 2.6	–	–	–	–	–
III γ	314 ± 2.6	288 ± 14	26	814 ^a	465	13 ± 16.5	0.3
V γ	316 ± 3.9	306 ± 8.5	10	825	482	34 ± 4.1	0.8
IX γ	317 ± 2.1	307 ± 10	10	836	483	35 ± 3.1	0.8
X γ	313 ± 1.9	302 ± 5.6	11	783	478	28 ± 39.5	0.7

^aValue estimated by the average of the other temperatures

The inherited zircon population of these granites suggest that they are melting restites of units with Cadomian (650 to 550 Ma) and Upper Cambrian–Lower Ordovician (495 to 470 Ma) ages. In addition, these zircon age distributions reveal a protolith affinity with the Douro-Beiras Supergroup, as retrieved from the Spanish sector. It should also be noted a remarkable contribution of Upper Cambrian–Lower Ordovician ages, which point out to the contribution of metaigneous rocks of the Ollo de Sapo formation

Combining the U–Pb zircon ages with the U–Pb apatite ages and their respective closure temperatures, it was possible, for the first time, to quantitatively constrain the emplacement conditions of the FCR–LAC granites. Zircon (317 ± 2.1–313 ± 1.9 Ma) and apatite (307 ± 10–288 ± 14 Ma) enable the calculation of cooling rates ranging from 13 to 35 °C Ma⁻¹. The closure temperatures of both geothermometers (zircon and apatite) allowed to estimate the emplacement of the studied granites at approximately 8 km of depth due to a fast exhumation mechanism. Such emplacement conditions are compatible with the transpressive shearing associated with the movement of the Juzbado–Penalva do Castelo shear zone, the most likely mechanism for the exhumation of the FCR–LAC (Pereira et al. 2017).

This novel application of zircon and apatite as petrochronometers, particularly in the CIZ where this approach was used for the first time, has proven to be useful in constraining the emplacement conditions (e.g., crystallization temperatures, cooling and exhumation rates) of syn-tectonic, S-type granitoids. This new type of approach is, therefore, important to understand the behavior of the continental crust during orogenic processes.

Acknowledgements J. A. Ferreira thanks the financial support attributed by Fundação para a Ciência e Tecnologia (FCT) doctoral Grant (PD/BD/114486/2016). We would like to acknowledge the University of Portsmouth for providing technical support during sample preparation and the analytical facilities for the SEM and LA-ICP-MS analyses. This publication was supported by FCT—Project UID/GEO/50019/2019—Instituto Dom Luiz. The authors are grateful to the Editor in Chief Prof. Wolf-Christian Dullo, the Topic Editor Prof.

J. F. Moyen, and reviewers Ícaro Dias da Silva and Marc Poujol for providing very helpful and insightful reviews with many comments and suggestions, therefore, improving our work.

References

- Aleinikoff JN, Schenck WS, Plank MO et al (2006) Deciphering igneous and metamorphic events in high-grade rocks of the Wilmington Complex, Delaware: morphology, cathodoluminescence and backscattered electron zoning, and SHRIMP U–Pb geochronology of zircon and monazite. *Bull Geol Soc Am* 118:39–64. <https://doi.org/10.1130/B25659.1>
- Alves Ribeiro J, Monteiro-Santos FA, Pereira MF et al (2017) Magnetotelluric imaging of the lithosphere across the Variscan Orogen (Iberian autochthonous domain, NW Iberia). *Tectonics* 36:3065–3080. <https://doi.org/10.1002/2017TC004593>
- Annen C, Scaillet B, Sparks RSJ (2006) Thermal constraints on the emplacement rate of a large intrusive complex: the Manaslu Leucogranite, Nepal Himalaya. *J Petrol* 47:71–95
- Arenas R, Sánchez Martínez S, Díez Fernández R et al (2016) Allochthonous terranes involved in the Variscan suture of NW Iberia: a review of their origin and tectonothermal evolution. *Earth Sci Rev* 161:140–178. <https://doi.org/10.1016/J.EARSCIREV.2016.08.010>
- Ashwal LD, Tucker RD, Zinner EK (1999) Slow cooling of deep crustal granulites and Pb-loss in zircon. *Geochim Cosmochim Acta* 63:2839–2851. [https://doi.org/10.1016/S0016-7037\(99\)00166-0](https://doi.org/10.1016/S0016-7037(99)00166-0)
- Azevedo MR, Valle Aguado B (2013) Origem e instalação de Granitóides Variscos na Zona Centro-Ibérica. In: Dias R, Araújo A, Terrinha P, Kullberg JC (eds) *Geologia de Portugal, vol 1. Geologia Pré-mesozóica de Portugal*. Escolar Editora, Lisbon, pp 377–401
- Baksi AK (1994) Geochronological studies on whole-rock basalts, Deccan Traps, India: evaluation of the timing of volcanism relative to the KT boundary. *Earth Planet Sci Lett* 121:43–56. [https://doi.org/10.1016/0012-821X\(94\)90030-2](https://doi.org/10.1016/0012-821X(94)90030-2)
- Barbarin B (1988) Use of zircon typology for the study of some granites from the Massif Central, France. *Rend Soc Ital di Miner e Petrol* 43:463–476
- Belousova EA, Griffin WL, O'Reilly SY (2006) Zircon crystal morphology, trace element signatures and Hf isotope composition as a tool for petrogenetic modelling: examples from Eastern Australian granitoids. *J Petrol* 47:329–353. <https://doi.org/10.1093/ptetrology/egi077>
- Benisek A, Finger F (1993) Factors controlling the development of prism faces in granite zircons: a microprobe study. *Contrib Mineral Petrol* 114:441–451

- Bento dos Santos TM, Munhá JM, Tassinari CCG et al (2010) Thermochronology of central Ribeira Fold Belt, SE Brazil: petrological and geochronological evidence for long-term high temperature maintenance during Western Gondwana amalgamation. *Precambr Res* 180:285–298. <https://doi.org/10.1016/J.PRECAMRES.2010.05.002>
- Bento dos Santos TM, Munhá JM, Tassinari CCG et al (2011) Metamorphic PT evolution of granulites in the central Ribeira Fold Belt, SE Brazil. *Geosci J* 15:27–51. <https://doi.org/10.1007/s12303-011-0004-1>
- Bento dos Santos TM, Tassinari CCG, Fonseca PE (2014) Garnet–biotite diffusion mechanisms in complex high-grade orogenic belts: understanding and constraining petrological cooling rates in granulites from Ribeira Fold Belt (SE Brazil). *J S Am Earth Sci* 56:128–138. <https://doi.org/10.1016/J.JSAMES.2014.09.003>
- Cerling TE, Brown FH, Bowman JR (1985) Low-temperature alteration of volcanic glass: hydration, Na, K, ^{18}O and Ar mobility. *Chem Geol Isot Geosci Sect* 52:281–293. [https://doi.org/10.1016/0168-9622\(85\)90040-5](https://doi.org/10.1016/0168-9622(85)90040-5)
- Cherniak DJ, Watson EB (2000) Pb diffusion in zircon. *Contrib Mineral Petrol* 160:383–390. <https://doi.org/10.1007/s00410-009-0483-5>
- Cherniak DJ, Lanford WA, Ryerson FJ (1991) Lead diffusion in apatite and zircon using ion implantation and Rutherford backscattering techniques. *Geochim Cosmochim Acta* 55:1663–1673. [https://doi.org/10.1016/0016-7037\(91\)90137-T](https://doi.org/10.1016/0016-7037(91)90137-T)
- Chesley JT, Halliday AN, Snee LW et al (1993) Thermochronology of the Cornubian batholith in southwest England: implications for pluton emplacement and protracted hydrothermal mineralization. *Geochim Cosmochim Acta* 57:1817–1835. [https://doi.org/10.1016/0016-7037\(93\)90115-D](https://doi.org/10.1016/0016-7037(93)90115-D)
- Chew DM, Petrus JA, Kamber BS (2014) U–Pb LA–ICPMS dating using accessory mineral standards with variable common Pb. *Chem Geol*. <https://doi.org/10.1016/j.chemgeo.2013.11.006>
- Clemens JD (2003) S-type granitic magmas—petrogenetic issues, models and evidence. *Earth Sci Rev* 61:1–18. [https://doi.org/10.1016/S0012-8252\(02\)00107-1](https://doi.org/10.1016/S0012-8252(02)00107-1)
- Clemens JD, Stevens G (2016) Melt segregation and magma interactions during crustal melting: breaking out of the matrix. *Earth Sci Rev* 160:333–349. <https://doi.org/10.1016/j.earscirev.2016.07.012>
- Corfu F, Hanchar JM, Hoskin PWO, Kinny PD (2003) Atlas of zircon textures. *Rev Mineral Geochem* 53:469–500. <https://doi.org/10.2113/0530469>
- Corsini M, Rolland Y (2009) Late evolution of the southern European Variscan belt: exhumation of the lower crust in a context of oblique convergence. *Comptes Rendus Geosci* 341:214–223. <https://doi.org/10.1016/j.crte.2008.12.002>
- Costa MM, Neiva AMR, Azevedo MR, Corfu F (2014) Distinct sources for syntectonic Variscan granitoids: insights from the Aguiar da Beira region, Central Portugal. *Lithos* 196–197:83–98. <https://doi.org/10.1016/j.lithos.2014.02.023>
- Dallmeyer RD, Martínez Catalán JR, Arenas R et al (1997) Diachronous Variscan tectonothermal activity in the NW Iberian Massif: evidence from $^{40}\text{Ar}/^{39}\text{Ar}$ dating of regional fabrics. *Tectonophysics* 277:307–337. [https://doi.org/10.1016/S0040-1951\(97\)00035-8](https://doi.org/10.1016/S0040-1951(97)00035-8)
- Dias da Silva Í, Gómez-Barreiro J, Martínez Catalán JR et al (2017) Structural and microstructural analysis of the Retortillo Syncline (Variscan belt, Central Iberia). Implications for the Central Iberian Orocline. *Tectonophysics* 717:99–115. <https://doi.org/10.1016/j.tecto.2017.07.015>
- Dias da Silva Í, Pereira MF, Silva JB, Gama C (2018) Time–space distribution of silicic plutonism in a gneiss dome of the Iberian Variscan Belt: the Évora Massif (Ossa-Morena Zone, Portugal). *Tectonophysics* 747–748:298–317. <https://doi.org/10.1016/j.tecto.2018.10.015>
- Dias G, Leterrier J, Mendes A et al (1998) U–Pb zircon and monazite geochronology of post-collisional Hercynian granitoids from the Central Iberian Zone (Northern Portugal). *Lithos* 45:349–369. [https://doi.org/10.1016/S0024-4937\(98\)00039-5](https://doi.org/10.1016/S0024-4937(98)00039-5)
- Dias R, Ribeiro A, Romão J et al (2016) A review of the arcuate structures in the Iberian Variscides; constraints and genetic models. *Tectonophysics* 681:170–194. <https://doi.org/10.1016/j.tecto.2016.04.011>
- Díaz-Azpiroz M, Barcos L, Balanyá JC et al (2014) Applying a general triclinic transpression model to highly partitioned brittle–ductile shear zones: a case study from the Torcal de Antequera massif, external Betics, southern Spain. *J Struct Geol* 68:316–336. <https://doi.org/10.1016/J.JSG.2014.05.010>
- Díez Fernández R, Pereira MF (2016) Extensional orogenic collapse captured by strike-slip tectonics: constraints from structural geology and U–Pb geochronology of the Pinhel shear zone (Variscan orogen, Iberian Massif). *Tectonophysics* 691:290–310. <https://doi.org/10.1016/j.tecto.2016.10.023>
- Díez Fernández R, Pereira MF (2017) Strike-slip shear zones of the Iberian Massif: are they coeval? *Lithosphere* 9:726–744. <https://doi.org/10.1130/L648.1>
- Dodson MH (1973) Closure temperature in cooling geochronological and petrological systems. *Contrib Mineral Petrol* 40:259–274. <https://doi.org/10.1007/BF00373790>
- Escuder-Viruete J, Arenas R, Catalán JRM (1994) Tectonothermal evolution associated with Variscan crustal extension in the Tormes Gneiss Dome (NW Salamanca, Iberian Massif, Spain). *Tectonophysics* 238:117–138. [https://doi.org/10.1016/0040-1951\(94\)90052-3](https://doi.org/10.1016/0040-1951(94)90052-3)
- Fernández C, Czeck DM, Díaz-Azpiroz M (2013) Testing the model of oblique transpression with oblique extrusion in two natural cases: steps and consequences. *J Struct Geol* 54:85–102. <https://doi.org/10.1016/J.JSG.2013.07.001>
- Ferreira N, Iglesias M, Noronha F et al (1987) Granitoides da zona Centro-Ibérica e seu enquadramento geodinâmico. In: Bea F, Carmina A, Gonzalo JC, Plaza ML (eds) *Geología de los granitoides y rocas asociadas del Macizo Hespérico*. Editorial Rueda, Madrid, pp 37–53
- Gallien F, Mogessie A, Bjerg E et al (2010) Timing and rate of granulite facies metamorphism and cooling from multi-mineral chronology on migmatitic gneisses, Sierras de La Huerta and Valle Fértil, NW Argentina. *Lithos* 114:229–252. <https://doi.org/10.1016/j.lithos.2009.08.011>
- García Garzon J, Locutura J (1981) Datación por el método Rb/Sr de los granitos de Lumbrales Sobradillo y Villar de Ciervos-Puerto Seguro. *Boletín Geol Min* 92(1):68–72
- García-Arias M, Díez-Montes A, Villaseca C, Blanco-Quintero IF (2018) The Cambro-Ordovician Olla de Sapo magmatism in the Iberian Massif and its Variscan evolution: a review. *Earth Sci Rev* 176:345–372. <https://doi.org/10.1016/j.earscirev.2017.11.004>
- Gutiérrez-Alonso G, Fernández-Suárez J, Gutiérrez-Marco JC et al (2007) U–Pb depositional age for the upper Barrios Formation (Armorican Quartzite facies) in the Cantabrian zone of Iberia: implications for stratigraphic correlation and paleogeography. *Spec Pap Soc Am* 423:287–296
- Gutiérrez-Alonso G, Collins AS, Fernández-Suárez J et al (2015) Dating of lithospheric buckling: $^{40}\text{Ar}/^{39}\text{Ar}$ ages of syn-orocline strike-slip shear zones in northwestern Iberia. *Tectonophysics* 643:44–54. <https://doi.org/10.1016/j.tecto.2014.12.009>
- Gutiérrez-Alonso G, Fernández-Suárez J, López-Carmona A, Gärtner A (2018) Exhuming a cold case: the early granodiorites of the northwest Iberian Variscan belt—a Viséan magmatic flare-up? *Lithosphere* 10:194–216. <https://doi.org/10.1130/L706.1>
- Hodges KV, Heinrich DH, Karl KT (2003) Geochronology and thermochronology in orogenic systems. *Treatise Geochem* 3:263–292. <https://doi.org/10.1016/B0-08-043751-6/03024-3>

- Iglesias M, Ribeiro A (1981) La zone de cisaillement ductile de Juzbado (Salamanca)–Penalva Do Castelo (Viseu): un linéament ancien réactivé pendant l'orogénese hercynienne? *Comun dos Serviços Geol Port* 67(1):89–93
- Jackson SE, Pearson NJ, Griffin WL, Belousova EA (2004) The application of laser ablation-inductively coupled plasma-mass spectrometry to in situ U–Pb zircon geochronology. *Chem Geol* 211:47–69
- Jadamec MA, Turcotte DL, Howell P (2007) Analytic models for orogenic collapse. *Tectonophysics* 435:1–12. <https://doi.org/10.1016/j.tecto.2007.01.007>
- Jochum KP, Weis U, Stoll B et al (2011) Determination of reference values for NIST SRM 610–617 glasses following ISO guidelines. *Geostand Geoanal Res* 35:397–429
- Köksal S, Cemal Göncüoğlu M, Toksoy-Köksal F et al (2008) Zircon typologies and internal structures as petrogenetic indicators in contrasting granitoid types from central Anatolia, Turkey. *Mineral Petrol* 93:185–211. <https://doi.org/10.1007/s00710-007-0228-y>
- Kroner U, Romer RL (2013) Two plates—many subduction zones: the Variscan orogeny reconsidered. *Gondwana Res* 24:298–329. <https://doi.org/10.1016/j.gr.2013.03.001>
- Lopez-Sanchez MA, Aleinikoff JN, Marcos A et al (2016) An example of low-Th/U zircon overgrowths of magmatic origin in a late orogenic Variscan intrusion: the San Ciprián massif (NW Spain). *J Geol Soc Lond* 173:282–291. <https://doi.org/10.1144/jgs2015-071>
- Ludwig KR (2003) User's manual for Isoplot/Ex version 300, a geochronological toolkit for Microsoft Excel. Geochronology Center Special Publication, Berkeley, p 72
- Macedo CCR (1988) Granitóides, Complexo Xisto-Grauváquico e Ordovícico na região entre Trancoso e Pinhel—geologia, petrologia, geocronologia. Universidade de Coimbra
- Martínez Catalán JR, Rubio Pascual FJ, Montes AD et al (2014) The late Variscan HT/LP metamorphic event in NW and Central Iberia: relationships to crustal thickening, extension, orocline development and crustal evolution. *Geol Soc Lond Spec Publ* 405:225–247. <https://doi.org/10.1144/SP405.1>
- Mata J, Alves CF, Martins L et al (2015) $^{40}\text{Ar}/^{39}\text{Ar}$ ages and petrogenesis of the West Iberian Margin onshore magmatism at the Jurassic–Cretaceous transition: geodynamic implications and assessment of open-system processes involving saline materials. *Lithos* 236–237:156–172
- Mateus A, Munhá J, Ribeiro A et al (2016) U–Pb SHRIMP zircon dating of high-grade rocks from the upper allochthonous terrane of Bragança and Morais Massifs (NE Portugal); geodynamic consequences. *Tectonophysics* 675:23–49. <https://doi.org/10.1016/j.tecto.2016.02.048>
- Matte P (1991) Accretionary history and crustal evolution of the Variscan belt in Western Europe. *Tectonophysics* 196:309–337
- Meert JG, Hall C, Nédélec L, Madison Razanatseho MO (2001) Cooling of a late-syn orogenic pluton: evidence from laser K-feldspar modelling of the Carion Granite, Madagascar. *Gondwana Res* 4:541–550. [https://doi.org/10.1016/S1342-937X\(05\)70353-1](https://doi.org/10.1016/S1342-937X(05)70353-1)
- Miyazaki T, Santosh M (2005) Cooling history of the Puttetti alkali syenite pluton, southern India. *Gondwana Res* 8:567–574. [https://doi.org/10.1016/S1342-937X\(05\)71156-4](https://doi.org/10.1016/S1342-937X(05)71156-4)
- Möller A, O'Brien PJ, Kennedy A, Kröner A (2003) The use and abuse of Th–U ratios in the interpretation of zircon. In: Geophysical research abstracts, European Geosciences Union, p 12113
- Munhá JMU, Cordani UG, Tassinari CG, Palácios T (2005) Petrologia e Termocronologia de Gnaisses Migmatíticos da Faixa de Dobramentos Araçuaí (Espírito Santo, Brasil). *Rev Bras Geociências* 35:123–134
- Nabelek PI, Hofmeister AM, Whittington AG (2012) The influence of temperature-dependent thermal diffusivity on the conductive cooling rates of plutons and temperature-time paths in contact aureoles. *Earth Planet Sci Lett* 317–318:157–164. <https://doi.org/10.1016/j.epsl.2011.11.009>
- Nance RD, Gutiérrez-Alonso G, Keppie JD et al (2010) Evolution of the Rheic Ocean. *Gondwana Res* 17:194–222. <https://doi.org/10.1016/j.gr.2009.08.001>
- Orejana D, Merino Martínez E, Villaseca C, Andersen T (2015) Ediacaran–Cambrian paleogeography and geodynamic setting of the Central Iberian Zone: constraints from coupled U–Pb–Hf isotopes of detrital zircons. *Precamb Res* 261:234–251. <https://doi.org/10.1016/j.precamres.2015.02.009>
- Pastor-Galán D, Dias da Silva ÍF, Groenewegen T, Krijgsman W (2019) Tangled up in folds: tectonic significance of superimposed folding at the core of the Central Iberian curve (West Iberia). *Int Geol Rev* 61:240–255. <https://doi.org/10.1080/00206814.2017.1422443>
- Pereira I, Dias R, Bento dos Santos T, Mata J (2017) Exhumation of a migmatite complex along a transpressive shear zone: inferences from the Variscan Juzbado–Penalva do Castelo Shear Zone (Central Iberian Zone). *J Geol Soc Lond* 174:1004–1018. <https://doi.org/10.1144/jgs2016-159>
- Pereira MF, Díez Fernández R, Gama C et al (2018) S-type granite generation and emplacement during a regional switch from extensional to contractional deformation (Central Iberian Zone, Iberian autochthonous domain, Variscan Orogeny). *Int J Earth Sci* 107:251–267. <https://doi.org/10.1007/s00531-017-1488-3>
- Pochon A, Poujol M, Gloaguen E et al (2016) U–Pb LA-ICP-MS dating of apatite in mafic rocks: evidence for a major magmatic event at the Devonian–Carboniferous boundary in the Armorican Massif (France). *American Mineralogist* 101(11):2430–2442. <https://doi.org/10.2138/am-2016-5736>
- Pupin JP (1980) Zircon and granite petrology. *Contrib Mineral Petrol* 73:207–220. <https://doi.org/10.1007/BF00381441>
- Rey P, Vanderhaeghe O, Teyssier C (2001) Gravitational collapse of the continental crust: definition, regimes and modes. *Tectonophysics* 342:435–449. [https://doi.org/10.1016/S0040-1951\(01\)00174-3](https://doi.org/10.1016/S0040-1951(01)00174-3)
- Ribeiro ML (2001) Carta geológica simplificada do Parque Arqueológico do vale do Côa: Escala 1:80.000: Notícia explicativa, p 71
- Ribeiro A, Munhá J, Dias R, Mateus A, Pereira E, Ribeiro L, Fonseca P, Araújo A, Oliveira J, Romão J, Chaminé H, Coke C, Pedro J (2007) Geodynamic evolution of the SW Europe Variscides. *Tectonics* 26(6):1–24. <https://doi.org/10.1029/2006TC002058>
- Roda-Robles E, Vieira R, Lima A, Pesquera-Pérez A (2009) Petrogenetic links between granites and pegmatites in the Fregeneda–Almendra area (Salamanca, Spain and Guarda, Portugal): new insights from $^{40}\text{Ar}/^{39}\text{Ar}$ dating in micas. *Estud Geol* 19:305–310
- Roda-Robles E, Villaseca C, Pesquera A et al (2018) Petrogenetic relationships between Variscan granitoids and Li–(FP)-rich aplite-pegmatites in the Central Iberian Zone: geological and geochemical constraints and implications for other regions from the European Variscides. *Ore Geol Rev* 95:408–430. <https://doi.org/10.1016/j.oregeorev.2018.02.027>
- Rodrigues JF, Bento dos Santos T, Castro P, et al (2013) Deformação não-coaxial na Faixa Metamórfica Porto-Viseu Détachement extensional ou par thrust/underthrust contraccional. In: 9ª Conferência Anual do GGET/SGP. Estremoz, pp 131–134
- Rubatto D (2017) Zircon: the metamorphic mineral. *Rev Mineral Geochem* 83:261–295. <https://doi.org/10.2138/rmg.2017.83.9>
- Rubatto D, Gebauer D (2000) Use of cathodoluminescence for U–Pb zircon dating by ion microprobe: some examples from the Western Alps. *Cathodoluminescence in geosciences*. Springer, New York, pp 373–400

- Sá A, Meireles C, Coke C, Gutiérrez-Marco J (2005) Unidades litoestratigráficas do Ordovícico da região de Trás-os-Montes (Zona Centro Ibérica). *Comun Geol* 92:31–74
- Schaltegger U, Davies JHFL (2017) Petrochronology of zircon and baddeleyite in igneous rocks: reconstructing magmatic processes at high temporal resolution. *Rev Mineral Geochem* 83(1):297–328. <https://doi.org/10.2138/rmg.2017.83.10>
- Schoene B, Bowring SA (2006) U–Pb systematics of the McClure Mountain syenite: thermochronological constraints on the age of the $^{40}\text{Ar}/^{39}\text{Ar}$ standard MMhb. *Contrib Mineral Petrol* 151:615–630. <https://doi.org/10.1007/s00410-006-0077-4>
- Schoene B, Bowring SA (2007) Determining accurate temperature–time paths from U–Pb thermochronology: an example from the Kaapvaal craton, southern Africa. *Geochim Cosmochim Acta* 71:165–185. <https://doi.org/10.1016/j.gca.2006.08.029>
- Schulmann K, Schaltegger U, Jezek J et al (2002) Rapid burial and exhumation during orogeny: thickening and synconvergent exhumation of thermally weakened and thinned crust (Variscan orogen in Western Europe). *Am J Sci* 302:856–879. <https://doi.org/10.2475/ajs.302.10.856>
- Schulmann K, Lexa O, Štípská P et al (2008) Vertical extrusion and horizontal channel flow of orogenic lower crust: key exhumation mechanisms in large hot orogens? *J Metamorph Geol* 26:273–297. <https://doi.org/10.1111/j.1525-1314.2007.00755.x>
- Scibiorski E, Tohver E, Jourdan F (2015) Rapid cooling and exhumation in the western part of the Mesoproterozoic Albany–Fraser Orogen, Western Australia. *Precamb Res* 265:232–248. <https://doi.org/10.1016/j.precamres.2015.02.005>
- Siégl C, Bryan SE, Allen CM, Gust DA (2018) Use and abuse of zircon-based thermometers: a critical review and a recommended approach to identify antecrystic zircons. *Earth Sci Rev* 176:87–116. <https://doi.org/10.1016/j.earscirev.2017.08.011>
- Silva A, Ribeiro ML (2000) Carta Geológica Simplificada do Parque Arqueológico do Vale do Côa. In: Parque Arq. Vila Nova de Foz Côa
- Sláma J, Kosler J, Crowley JL et al (2007) Plesovice zircon—a new natural standard for U–Pb and Hf isotopic microanalysis. *Geochim Cosmochim Acta* 71:A947–A947
- Sousa MB, Sequeira AJD (1993) O limite Precâmbrico–Câmbrico na Zona Centro Ibérica, em Portugal. *XII Reun Geol do Oeste Penins* 1:17–28
- Spear FS, Parrish RR (1996) Petrology and cooling rates of the Valhalla Complex, British Columbia, Canada. *J Petrol* 37:733–765
- Steenken A, Siegesmund S, Heinrichs T, Fügenschuh B (2002) Cooling and exhumation of the Rieserferner Pluton (Eastern Alps, Italy/Austria). *Int J Earth Sci* 91:799–817. <https://doi.org/10.1007/s00531-002-0260-4>
- Thomson SN, Gehrels GE, Ruiz J, Buchwaldt R (2012) Routine low-damage apatite U–Pb dating using laser ablation–multicollector–ICPMS. *Geochim Geophys Geosyst*. <https://doi.org/10.1029/2011gc003928>
- Tsuchiya N, Fujino K (2000) Evaluation of cooling history of the Quaternary Takidani Pluton using thermoluminescence technique. *Proc World Geotherm Congr 2000*:3939–3944
- Valle Aguado B, Azevedo MR, Schaltegger U et al (2005) U–Pb zircon and monazite geochronology of Variscan magmatism related to syn-convergence extension in Central Northern Portugal. *Lithos* 82:169–184. <https://doi.org/10.1016/j.lithos.2004.12.012>
- Valle Aguado B, Azevedo MR, Nolan J et al (2017) Granite emplacement at the termination of a major Variscan transcurrent shear zone: the late collisional Viseu batholith. *J Struct Geol* 98:15–37. <https://doi.org/10.1016/j.jsg.2017.04.002>
- Vanderhaeghe O (2009) Migmatites, granites and orogeny: flow modes of partially-molten rocks and magmas associated with melt/solid segregation in orogenic belts. *Tectonophysics* 477:119–134. <https://doi.org/10.1016/j.tecto.2009.06.021>
- Vanderhaeghe O, Teyssier C (2001) Crustal-scale rheological transitions during late-orogenic collapse. *Tectonophysics* 335:211–228. [https://doi.org/10.1016/S0040-1951\(01\)00053-1](https://doi.org/10.1016/S0040-1951(01)00053-1)
- Vanderhaeghe O, Kruckenberg S, Gerbault M et al (2018) Crustal-scale convection and diapiric upwelling of a partially molten orogenic root (Naxos dome, Greece). *Tectonophysics* 746:459–469. <https://doi.org/10.1016/j.tecto.2018.03.007>
- Vavra G (1990) On the kinematics of zircon growth and its petrogenetic significance: a cathodoluminescence study. *Contrib Mineral Petrol* 106:90–99. <https://doi.org/10.1007/BF00306410>
- Vavra G (1993) A guide to quantitative morphology of accessory zircon. *Chem Geol* 110:15–28. [https://doi.org/10.1016/0009-2541\(93\)90245-E](https://doi.org/10.1016/0009-2541(93)90245-E)
- Vermeesch P (2018) IsoplotR: a free and open toolbox for geochronology. *Geosci Front* 9(5):1479–1493. <https://doi.org/10.1016/j.gsf.2018.04.001>
- Vieira R (2010) Aplitepegmatitos com Elementos Raros da Região entre Almendra (Vila Nova de Foz Côa) e Barca dAlva (Figueira de Castelo Rodrigo) Campo Aplitepegmatítico da Fregeneda-Almendra
- Villar Alonso P, Fernández Ruiz J, Bellido F et al (2000) Memoria del mapa geológico de España 1:50,000, Lumbrales (Hoja 475). In: Série magna, 1^ª e d, 2^ªsérie. Madrid
- Villaras A, Couzinié OLS, Mintrone JFMM (2018) Plutons and domes: the consequences of anatectic magma extraction—example from the southeastern French Massif Central. *Int J Earth Sci* 107:2819–2842. <https://doi.org/10.1007/s00531-018-1630-x>
- Villaseca C, Barbero L, Rogers G (1998) Crustal origin of Hercynian peraluminous granitic batholiths of Central Spain: petrological, geochemical and isotopic (Sr, Nd) constraints. *Lithos* 43:55–79. [https://doi.org/10.1016/S0024-4937\(98\)00002-4](https://doi.org/10.1016/S0024-4937(98)00002-4)
- Watson EB, Harrison TM (1983) Zircon saturation revisited: temperature and composition effects in a variety of crustal magma types. *Earth Planet Sci Lett* 64:295–304. [https://doi.org/10.1016/0012-821X\(83\)90211-X](https://doi.org/10.1016/0012-821X(83)90211-X)
- Watson EB, Wark DA, Thomas JB (2006) Crystallization thermometers for zircon and rutile. *Contrib Mineral Petrol* 151:413–433. <https://doi.org/10.1007/s00410-006-0068-5>
- Whittington AG, Hofmeister AM, Nabelek PI (2009) Temperature-dependent thermal diffusivity of the Earth’s crust and implications for magmatism. *Nature* 458:319–321. <https://doi.org/10.1038/nature07818>
- Wiedenbeck M, Allé P, Corfu F et al (1995) Three natural zircon standards for U–Th–Pb, Lu–Hf, trace element and REE analyses. *Geostand Newsl* 19:1–23. <https://doi.org/10.1111/j.1751-908X.1995.tb00147.x>
- Williams IS, Buick IS, Cartwright I (1996) An extended episode of early mesoproterozoic metamorphic fluid flow in the Reynolds Range, central Australia. *J Metamorph Geol* 14:29–47. <https://doi.org/10.1111/j.1525-1314.1996.00029.x>
- Yakymchuk C, Kirkland CL, Clark C (2018) Th/U ratios in metamorphic zircon. *J Metamorph Geol* 36:715–737. <https://doi.org/10.1111/jmg.12307>
- Yuguchi T, Sueoka S, Iwano H et al (2017) Spatial distribution of the apatite fission-track ages in the Toki granite, central Japan: exhumation rate of a Cretaceous pluton emplaced in the East Asian continental margin. *Isl Arc* 26:1–4. <https://doi.org/10.1111/iar.12219>
- Žák J, Verner K, Finger F et al (2011) The generation of voluminous S-type granites in the Moldanubian unit, Bohemian Massif, by rapid isothermal exhumation of the metapelitic middle crust. *Lithos* 121:25–40. <https://doi.org/10.1016/j.lithos.2010.10.002>
- Zhang H, Harris N, Parrish R et al (2004) Causes and consequences of protracted melting of the mid-crust exposed in the North Himalayan antiform. *Earth Planet Sci Lett* 228:195–212. <https://doi.org/10.1016/J.EPSL.2004.09.031>